Research Signpost
37/661 (2), Fort P.O., Trivandrum-695 023, Kerala, India

Bubble and Particle Dynamics in Acoustic Fields: Modern Trends and Applications, 2005:
ISBN: 81-7736-284-4 Editor: Alexander A. Doinikov

Bubble dynamics in therapeutic ultrasound

R. Glynn Holt and Ronald A. Roy
Department of Aerospace and Mechanical Engineering, Boston University
110 Cummington St., Boston, MA 02215, USA

Abstract

Rapid hyperthermia resulting in tissue necrosis has proven to be a useful therapeutic modality for clinical application of high-intensity focused ultrasound. At therapeutic intensities, the hyperthermia is often accompanied by bubble activity. In vitro and in vivo experiments alike have shown that under certain conditions bubble activity can give rise to a doubling of the heating rate. With a view towards harnessing the energy-concentrating effects of bubbles to do useful clinical work, we report the results of experiments and modeling for the dynamic and thermal behavior of bubbles subjected to 1-megahertz ultrasound at megapascal pressures. The dominant

Correspondence/Reprint request: Dr. R. Glynn Holt, Department of Aerospace and Mechanical Engineering Boston University, 110 Cummington St., Boston, MA 02215, USA. E-mail: rgholt@bu.edu

heating mechanism depends on bubble size, medium shear viscosity number and frequency-dependent acoustic attenuation. The bubble size distribution, in turn, depends on insonation control parameters (acoustic pressure, pulse duration), medium properties (notably dissolved gas concentration) and bubble-destroying shape instabilities. The evidence obtained so far points to a range of control parameters for which bubble-enhanced heating can be assured, while mitigating the effects on the primary acoustic field.

1. Introduction

It is well known that short-duration pulses of focused ultrasound can be used to form images of tissue and organ structure deep within the body. If the duration of the ultrasound and the intensity at the focus are increased significantly, sound absorption results in localized temperature elevation, leading to cell death. A prolate ellipsoidal lesion of order 2-mm width and 2-cm length results, and the surrounding tissue is largely unharmed. This concept of using *high-intensity focused ultrasound* (HIFU) to effect *focused ultrasound surgery* (FUS), depicted in Fig. 1.1, is rapidly gaining in popularity. A growing number of pre-clinical studies and clinical trials are under way, and a number of new devices have received FDA approval and/or are on the market. Applications envisioned include transcutaneous and intra-operative hemostasis [1,2], tumor ablation [3], hemolysis [4,5,6,7], drug transport [8], especially in the context of thrombolysis [9,10,11,12,13,14], and the list continues to increase. Early clinical successes have been documented, however many HIFU therapy systems suffer from a common set of limitations related to excessive treatment time, control of lesion size and shape, and targeting. We believe that many of these limitations can be minimized or overcome by a thorough study of acoustic cavitation physics.

Acoustic cavitation is often the result of the application of high-intensity ultrasound in a biomedical context. There are sound reasons, both experimental

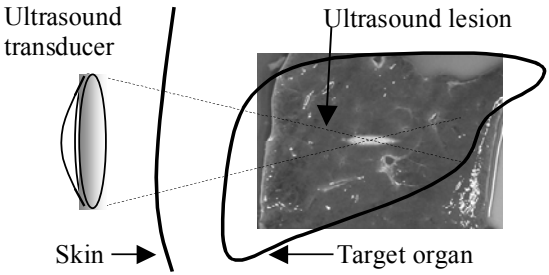

Figure 1.1. Focused Ultrasound Surgery

and theoretical, for defining therapeutic and diagnostic operating conditions in order to minimize bubble activity [15,16,17]. Most of the arguments boil down to the fact that bubbles perform a very efficient and highly nonlinear conversion of acoustical energy to mechanical motion. In therapeutic ultrasound, bubbles formed in the propagation path may inhibit deposition of acoustic energy because they scatter and absorb much of the energy before it can reach the target area, a process often referred to as 'screening' or 'shielding'.

However, there are therapeutic situations in which it is desirable to excite cavitation. Such is the case in the field of ultrasound surgery using high-intensity focused ultrasound (HIFU), where the goal is to produce irreversible necrosis deep into the tissue with minimal damage in the intervening path (as reviewed in [3], and highlighted in the special issue of IEEE UFFC, November 1996 [18]). If gross mechanical damage and tissue ablation is desired, then excitation of cavitation bubbles is the most efficacious (if also unavoidable) method (for example [19,20,21,22]). Most investigators have argued that cavitation is to be avoided, since it has typically led to unpredictable thermal results [23,24,25]. However, it has been argued [26,27] that with a combination of experiment and numerical modeling of the instability processes, bubble-enhanced heating (observed in [28,29,30,31]) is a controllable and thus desirable modality for HIFU.

Recently several groups [22,32,33) have employed cavitation with therapeutic ultrasound to achieve a variety of clinical ends. At least two groups [34,35] have explicitly initiated cavitation for use in HIFU, noting that cavitation allows them to use lower pressures to achieve the same heating, or that cavitation yields larger lesion sizes for the same pressures.

A key advantage to be gained by actively inducing but controlling cavitation is illustrated in Fig. 1.2. For low pressures ("linear" in the figure), the temperature rise is governed by linear absorption of the primary 1-MHz field, and is linearly proportional to the acoustic intensity, or the square of the acoustic amplitude [36,37,38]. Above some critical threshold pressure, the heating increases dramatically ("enhancement") coincident with the onset of cavitation. This enhanced heating yields (in the case of Fig. 1.2) approximately a five-fold increase in local temperature rise with respect to the primary heating from the ultrasound alone. As seen in Fig. 1.2, upon increasing the pressure at fixed duration of treatment (or equivalently on increasing duration at fixed pressure, not shown) saturation and shielding eventually occur. This shielding regime must be predicted or detected in order to ensure that its disadvantageous effects (unpredictable heating amount and location, and growth of the lesion in the pre-focal region) are minimized or avoided.

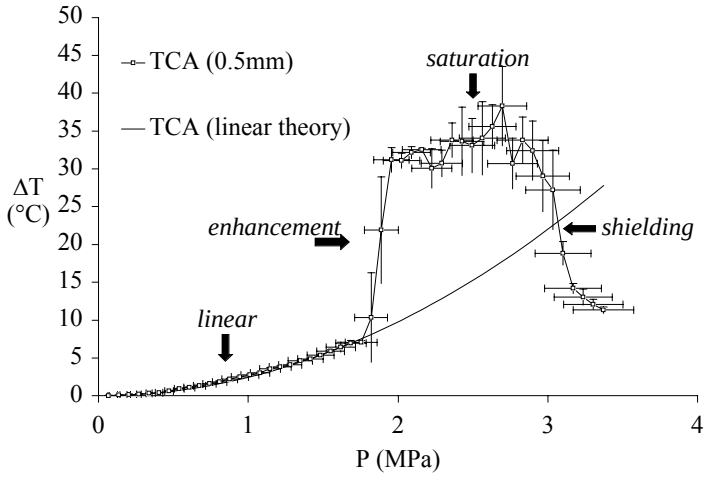

Figure 1.2. Peak temperature increase from ambient vs peak-positive acoustic pressure for an agar phantom subjected to 0.7 sec 1-MHz tonebursts. The thermocouple (TCA) location is measured relative to the acoustic axis. Each data point is the mean of 5 runs at that pressure, with 100 sec cooling between runs.

This Chapter describes the investigations and results of a program to study and utilize controlled acoustic cavitation to effect substantial increases in tissue heating rates, thereby reducing treatment time and pre-focal heating. Experiments with 1 MHz HIFU and thermal, acoustic and optical diagnostics highlight the effects of bubble dynamics and are presented in the Section 2 of this Chapter. We then turn to modeling the dominant bubble mechanics in Section 3 (nonlinear volume oscillations, shape and growth instabilities) to understand and ultimately control the biomedical effects of enhanced heating, lesion growth and sound scattering.

2. Experimental results

2.1 Enhanced heating

2.1.1 Baseline: Primary ultrasound heating

The goal of FUS is the rapid, controlled deposition of heat deep inside soft tissue. Typically this requires focused transducers in the MHz range. The measurements described in this Chapter were made using a transducer similar to that depicted in Fig. 2.1, which is a single element, piezoceramic spherically focused transducer (Sonic Concepts, Woodinville, WA) with a 6.24 cm focal length, a 7.0 cm aperture (an F-number close to unity, typical of many HIFU transducers), and a center frequency of 1.1 MHz.

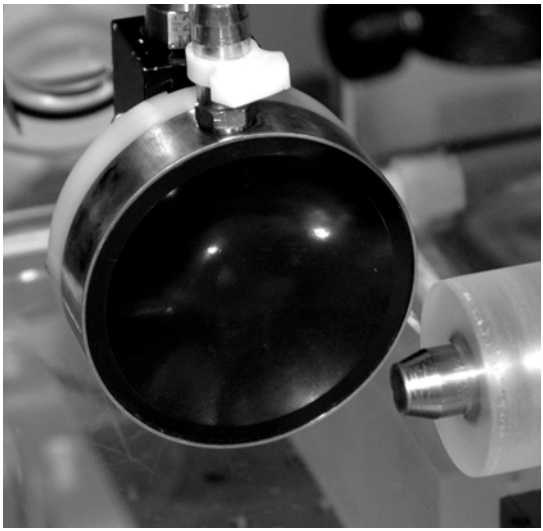

Figure 2.1. HIFU transducer shown in tank, with confocally mounted PCD transducer in foreground.

The acoustic field generated by such a transducer is well-described [39] by a modified Westervelt equation, accounting for the effects of diffraction, absorption, and nonlinearity [40]:

$$\left(\nabla^2 - \frac{1}{c^2}\frac{\partial^2}{\partial t^2}\right)p + \frac{\delta}{c^4}\frac{\partial^3 p}{\partial t^3} + \frac{\beta}{\rho c^4}\frac{\partial^2 p^2}{\partial t^2} = 0\,. \tag{1}$$

Here c is the sound speed, ρ is the density, δ is the acoustic diffusivity and is equal to $2c^2\alpha/\omega^2$, α is the local attenuation coefficient, ω the frequency, and $\beta = 1+B/2A$ is the (again local) coefficient of nonlinearity with B/A being the nonlinearity parameter of the medium. The model assumes a classical thermoviscous medium in which the absorption increases as the frequency squared, though for tissues the power law for absorption is closer to $f^{1.1}$. This will introduce error in the case of strongly nonlinear waves. Using a plane wave analysis of nonlinear propagation we estimated that the error in the heating term is less than 5% for focal peak pressures up to 2 MPa. Moreover, in our experiments the FUS fields generated acoustic cavitation before significant propagation nonlinearity set in, and once bubbles are present the model above is no longer strictly valid [41,42,43]. However, the propagation may be approximated by making an effective bubbly medium assumption, which we present later in this Chapter.

The heat deposited by absorption is given by the following expression, adapted from Pierce [44], which when combined with Eq. (1) gives the spatially-dependent ultrasonic power deposition per unit volume in a non-relaxing medium [45]:

$$q_{primary} = 2\alpha_{ABS} I = \frac{2\alpha_{ABS}}{\omega^2 \rho c} \left\langle \left(\frac{\partial p}{\partial t} \right)^2 \right\rangle . \tag{2}$$

Here, α_{ABS} refers to the local absorption coefficient of the medium, I is the local acoustic intensity, and the brackets denote time average over one acoustic cycle. The spatial distribution of the power density in Eq. (2) is plotted in Fig. 2.2 by integrating Eq. (1) for a single element focused bowl transducer of the type shown in Fig. 2.1.

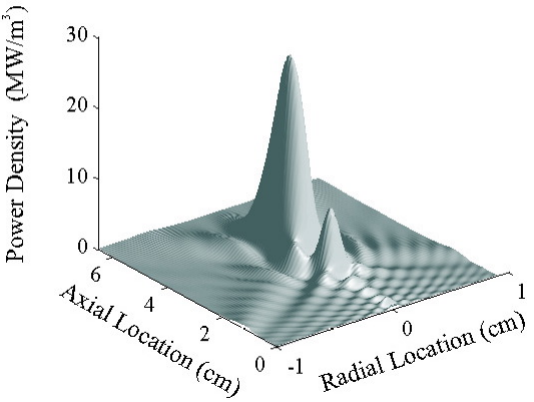

Figure 2.2. Calculated power density (from equations (1) and (2) due to primary acoustic absorption as a function of axial and radial location for a peak positive and negative acoustic pressure amplitude of 2.84 MPa and 2.64 MPa, respectively,at the focus.

In order to compare with our observations we must calculate the resulting temperature field. To model thermal transport in perfused tissue containing one or more larger blood vessels, we adapt the widely-used Pennes bioheat transfer equation [46] (BHTE), a form of the heat conduction equation with biologically relevant source and sink terms. The temperature field is split into two domains, perfused tissue and flowing blood, and can be expressed as

$$\rho_t C_t \frac{\partial T}{\partial t} = K_t \nabla^2 T - w_b C_b (T - T_\infty) + q \qquad (\textit{tissue domain}), \tag{3}$$

$$\rho_b C_b \frac{\partial T}{\partial t} = K_b \nabla^2 T - \rho_b C_b (\vec{u} \cdot \nabla T) + q \qquad \textbf{(}\textit{blood domain}\textbf{)}\textbf{,} \tag{4}$$

where ρ, C, and K are the density, specific heat and thermal conductivity with the subscripts t and b referring to tissue and blood domain, T_∞ refers to the temperature at large distances from the focus. w_b is the 'perfusion rate' which is an average mass flow rate accounting in an approximate way for blood flow in capillary beds. Finally $\vec{u}$ is the blood flow velocity. The blood flow field has two components: a fully developed parabolic flow (The Reynolds number Re = $2\rho r_0 U_0/\mu$ is less than 100 for many flow conditions of biomedical interest) plus an acoustic streaming flow. Thus, the total blood flow velocity field is written as

$$\vec{u} = \vec{u}_{ext} + \vec{u}_{str} = 2U_0 \left[1 - \left(\frac{r}{r_0} \right)^2 \right] + \vec{u}_{str} \,, \tag{5}$$

where $\vec{u}_{ext}$ represents parabolic Pouiseille flow and $\vec{u}_{str}$ is acoustic streaming, U_0 is the average velocity of the Pouiseille flow, μ is the shear viscosity, r is the radial distance from the flow axis, and r_0 is the radius of the vessel.

There is a considerable body of literature that develops the theoretical basis of acoustic streaming. The driving force derives from the acoustic field and is manifested as a spatially-dependent viscous momentum transfer from sound waves to fluid motion [47]. Much of the early work (Eckart [48] and others) assumed continuous plane waves and a second-order approximation, which is unsuitable for HIFU beams. Kamakura *et al*. [49,50] treat the currently relevant case of focused beams. We have included the full model equations here for completeness, and the interested reader is referred to [39] for more details and experiments with flow. For this Chapter we will ignore all flow effects on the primary heat deposition. We will thus compare our experiments with the results from Eq. (3), with w_b set to zero.

Figure 2.3 shows that experimentally measured heating is well described by the model of equations (1-3) for modest pressures. Thus, the expectation for heating from ultrasound is that the temperature achieved will be proportional to the square of the peak acoustic pressure.

2.1.2 Observations of enhanced heating

As reviewed in the Introduction there exist several observations of enhanced heating in the literature. This section will focus on in vitro observations in our lab [26, 27, 42, 43]. A generic schematic of the apparatus used to collect basic physical measurements is given in Fig. 2.4. Our experiments are conducted in tissue-mimicking phantom materials – for a more

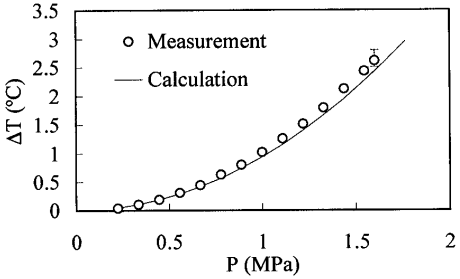

Figure 2.3. Comparison between measured and predicted temperature rises for a 5 s, 1 MHz HIFU insonation. The temperature was measured with a thermocouple embedded at the focus of a 1 MHz transducer in an Agar-graphite tissue phantom, and the calculation proceeds from Eq. (1-3) using the independently measured properties (sound speed, attenuation, specific heat, etc…) of the tissue phantom material. The artifactual boundary layer heating at the thermocouple has been accounted for in the measured values.

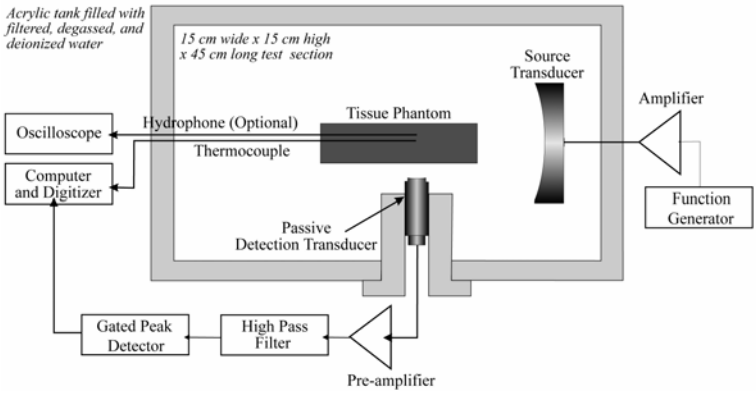

Figure 2.4 Schematic of experimental apparatus, incorporating a 1 MHz focused source, a thermocouple array, a needle hydrophone, and a 15 MHz focused detection transducer.

detailed description of their composition, physical properties and preparation the reader is referred to [51]. The primary diagnostics are temperature (from one or more thermocouples) and noise (from a passive transducer, described in the next section). Figure 1.2 has already highlighted the extra temperature rise as a function of acoustic pressure. Figure 2.5 shows the corresponding time domain results. The abrupt change from linear behavior to enhanced heating in both Fig. 1.2 and 2.5 is characteristic of a threshold-dependent phenomenon. The most likely culprit is acoustic cavitation.

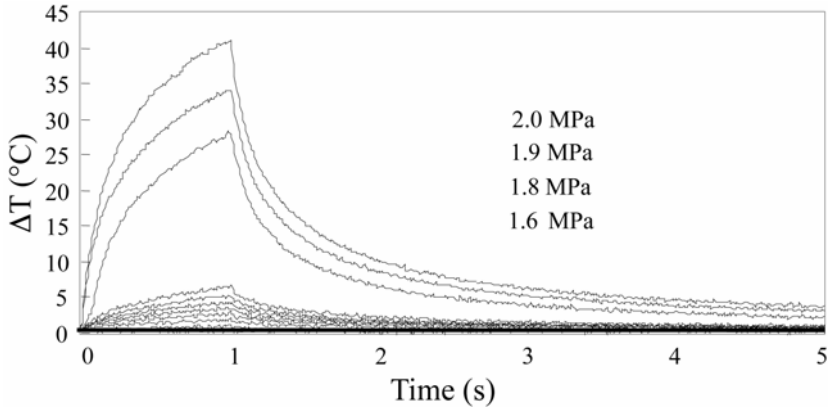

Figure 2.5 Temperature as a function of time for increasing acoustic pressure in approximately equal increments from 0.0 to 2.2 MPa. An enhanced heating effect is seen above 1.8 MPa where the peak temperature increases five-fold.

2.1.3 Noise emission correlations

In order to determine whether and what type of bubble activity is present when enhanced heating is observed, we listen for the noise generated by bubbles. While many methods exist for such bubble detection [52], we employed primarily a type of noise emission detection specific to detection of the high frequency broadband noise emitted by inertially collapsing bubbles. The features of such a passive cavitation detection system (PCD) are illustrated in Fig. 2.6. The tight confocal arrangement assures spatial specificity, and the high center frequency of the detector plus high-pass filtering ensure that the detector sees primarily broadband emissions of inertially collapsing bubbles. This specificity will help us to infer bubble size distributions in a later section.

Figure 2.7 illustrates the correlation of cavitation noise with enhanced heating. At a pressure (a) below the threshold for enhanced heating, the temperature rise is modest and the PCD indicates no cavitation noise. At 0.5 s at a higher pressure (b), the onset of enhanced heating is seen to correlate with the onset of noise. At a pressure above the threshold (c), both cavitation and enhanced heating begin immediately as the HIFU is turned on.

These results, summarized in Fig. 2.8 (for more results see [42]) allow us to reasonably infer that enhanced heating is always accompanied by inertial cavitation activity. In a later section we will see how this affects our conclusions of the dominant mechanisms for enhanced heating.

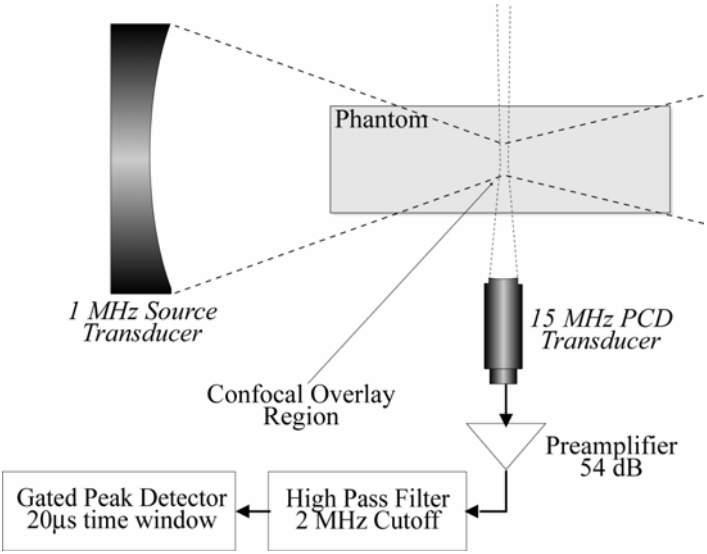

Figure 2.6 Schematic of PCD detection system.

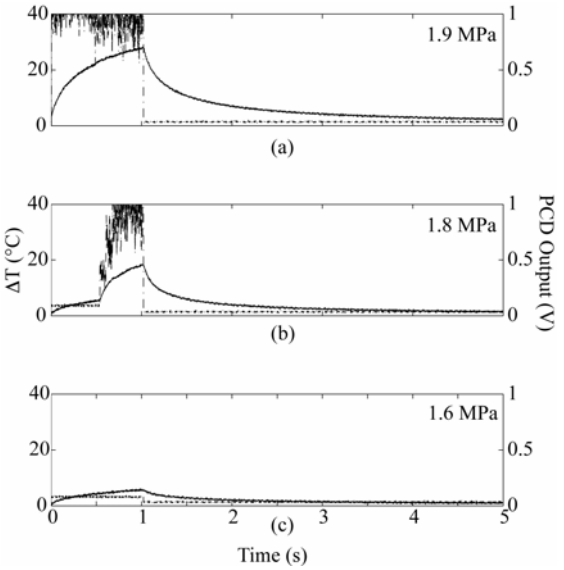

Figure 2.7 Temperature (solid line) and cavitation activity (dotted) as a function of time for a 1s insonation of 1MHz at three pressures.

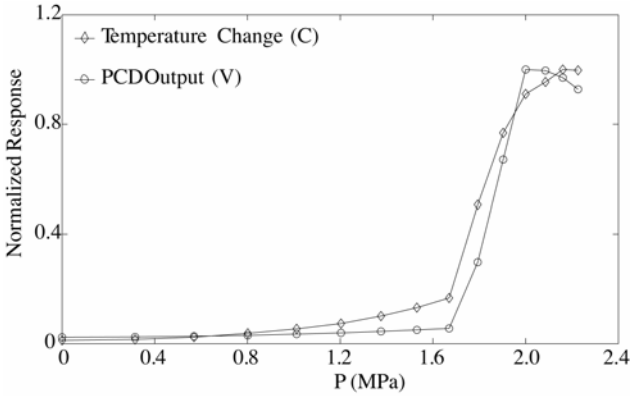

Figure 2.8 Temperature and cavitation activity vs pressure for 1MHz, 1s pulses of HIFU.

2.1.4 Dissolved gas dependence

The dissolved gas concentration in the body will, for blood and well-perfused tissues, be near saturation owing to constant diffusive replenishment in the lungs. However, for regions of poor circulation, or for not very vascular regions, the effective dissolved gas concentration may be lower than saturation. Also, for inertially collapsing bubbles, sonoluminescence research [53,54] has shown that in repetitive bubble motion only the inert gas component participates in diffusion. For all these reasons we investigate the dissolved gas dependence on the enhanced heating, shown in Fig. 2.9. There are two effects. First, the threshold for detectable enhanced heating is higher for lower dissolved gas concentration, presumably because the number of nuclei is less. Second, increasing the dissolved gas concentration increases the regularity of the effect (as indicated by the small error bars, which are the standard deviations of 5 runs at each pressure.) The likely explanation is that, at the higher concentrations, increasing bubble activity does not deplete the local concentration (which is diffusion limited, recall these are gel phantoms).

2.1.5 Nucleation via contrast agent

The body contains few nuclei, and tissue is harder to cavitate than blood. While our Agar-graphite phantom experiments (see Fig. 2.8 and 2.9, for example) exhibit a threshold for cavitation of approximately 1.5 MPa, these phantoms possess far more nuclei than in the body, where prompt cavitation (in contrast to boiling) from HIFU can be expected to occur at pressures more like 5 MPa [29]. In order to bring the cavitation threshold down and ensure more repeatable results, nuclei must be introduced. One of the most obvious

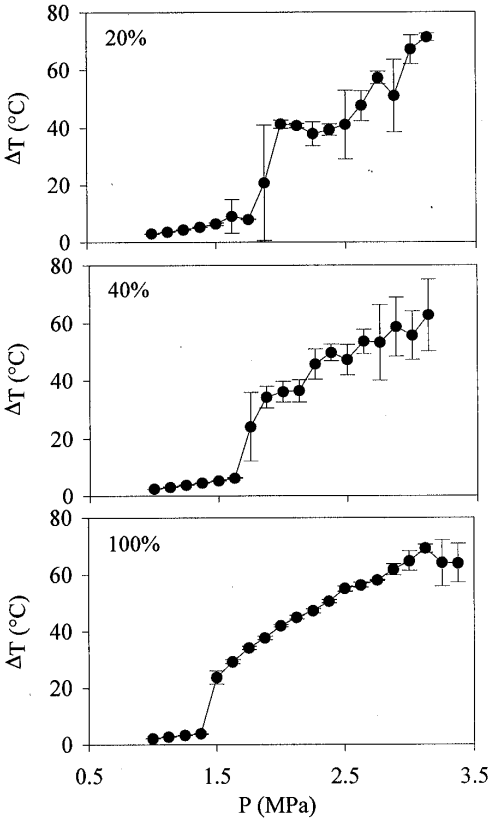

Figure 2.9. Peak temperature rise vs acoustic pressure for different dissolved gas concentrations.

ways to achieve nuclei introduction is via the use of microbubble contrast agents. Bubble-based contrast agents have been broadly used in medicine to improve ultrasound imaging [55]. The use of bubble-based contrast agents will also lower the cavitation threshold. The contrast agent we use in our experiments is Optison, a bubble-based contrast agent with mean diameter of 2.0-4.5 μm. The gas inside of Optison is octafluoropropane (C_3F_8), which has a very low solubility in water. The shell is made by denatured human serum albumin. For low Optison concentrations, inertial oscillations are required for Optison to result in enhanced heating. The inertial cavitation threshold for Optison is the upper bound for the threshold for Optison to break up. Once the Optison shell breaks up, its oscillation is going to be similar to a free bubble.

Optison was introduced via five flow-through tunnels of roughly 0.2mm each, separated by 0.3mm roughly. A syringe pump is used to inject Optison and a constant speed of 0.25ml/min is used. An Optison concentration of 500-800 bubbles/μl was used. The measured temperature results are showed in Fig. 2.10. The reference temperature rise is obtained by using water without Optison passing through the tunnel during insonation. Prefocus temperature rise is measured by a thermocouple which placed 3.8mm ahead of the focal thermocouple. Comparing the temperature rise at the focal region, we can see when Optison is used, the enhanced heating threshold is slightly lower. Compared to the reference temperature rise, it appears there are two temperature thresholds in the focal region when Optison is used. At a pressure value which is below the cavitation threshold value in the tissue phantom, we can see a clear enhanced heating when Optison is used at about 0.9 MPa. Then the second jump happens when the cavitation threshold value of the tissue phantom is reached at about 1.3MPa. For the reference temperature rise, only one temperature jump happens at the cavitation threshold.

The output of the PCD (not shown) indicates that the threshold for the Optison to oscillate inertially is about 1MPa, which is consistent with the first temperature jump in Fig. 2.10, also around 1MPa. Thus, for these clinically relevant but modest concentrations, Optison can enhance heating in the tissue phantom only after the pressure is above the inertial cavitation threshold of the Optison. The enhanced heating between the first temperature jump and the second temperature jump is caused by Optison solely and may be useful as a tool for controlled bubble enhanced heating. It seems clear that any method which can provide controlled nuclei would be essential for harnessing bubbles or HIFU applications.

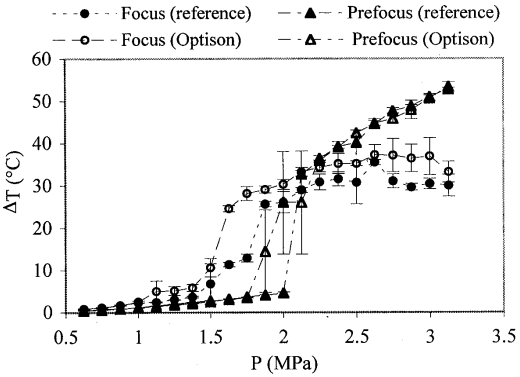

Figure 2.10. Peak temperature rise vs acoustic pressure for Optison-infused Agar-graphite tissue phantoms for a 1MHz, 1MPa, 1s insonation.

2.1.6 Laser-induced nanoparticle nucleation

The interaction of lasers with micro- and nanometer sized particles has received much recent attention in such diverse fields as optics [56], non-destructive testing [57], biomedical imaging [58] and various treatment scenarios involving selective cell death [59]. Pigmented particles, either naturally occurring in the retinal pigment epithelium, or as added to cells, have been shown to exhibit such large absorption rates when undergoing visible laser radiation that vapor bubbles form, expand and collapse ("microcavitation"), selectively killing only those cells containing the melanin particles [60,61,62]. True nanoparticles (250nm, 100nm, 40nm 10nm and 2nm gold particles [58]) have also shown microbubble formation in suspensions or cells when irradiated by visible laser pulses.

Motivated by these studies, an experiment was performed [63] to investigate whether at lower laser powers small nanometer-size vapor cavities might form which would then serve as nuclei for HIFU. Figure 2.11 shows a schematic of the experimental apparatus. In contrast to the Agar-graphite phantoms, we have employed an optically transparent acrylamide phantom in this experiment. Without any inclusions, the threshold for nucleation and subsequent inertial cavitation is higher than in the Agar-graphite phantoms [39]. The results (Fig. 2.12) show that the laser/particle assisted nucleation occurs at 0.9 MPa – the unassisted nucleation threshold for this experiment was about 5 MPa. Targeted imaging and therapy delivery are the potential benefits of this nucleation method.

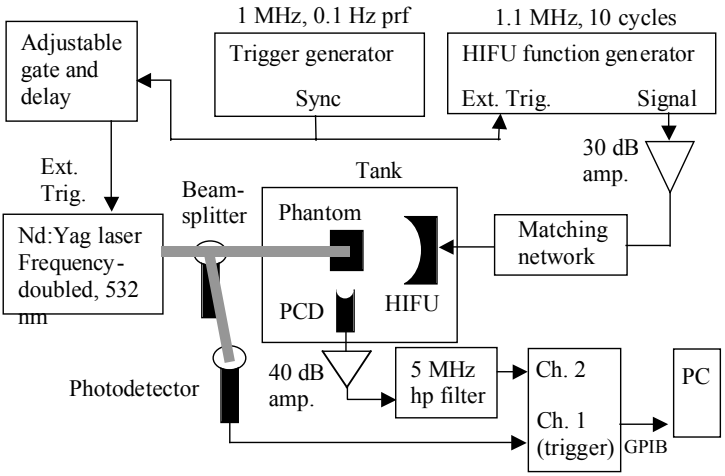

Figure 2.11. Experimental arrangement for simultaneous laser and HIFU irradiation of an 82 nm gold particle-bearing acrylamide tissue phantom.

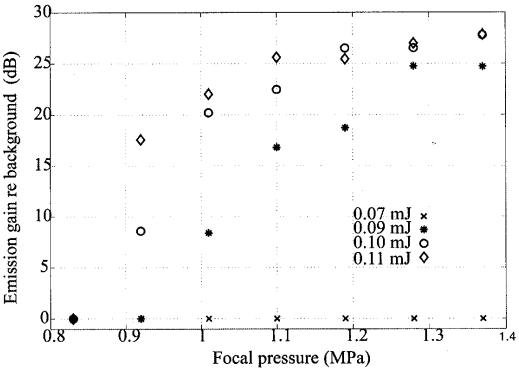

Figure 2.12. PCD output vs acoustic pressure for several laser intensities.

2.1.7 Imaging and hyperechogenicity

There is much interest in imaging the treatment area during FUS. While histology can clearly indicate the destroyed or lesioned tissue after experiments, of critical value to the treating physician is the *real-time* indication of the lesioned volume. There exist several efforts to achieve such a real-time indication, using both MRI and ultrasound modalities. Ultrasound, for reasons of expense and size, is the preferred modality; however, lesioned tissue per se indicates only relatively small changes in sound speed and attenuation. Most current literature and conferences report the appearance of a strongly hyperechogenic region in conventional ultrasound B-scans during HIFU treatment. This hyperechoic region has generally been taken as an indicator of the onset of cavitation and/or boiling, and is currently being used as an indicator of successful lesion formation. We believe that a hyperechogenic region is likely due to large gas and vapor (boiling) bubbles associated with extreme levels of cavitation activity and heating that has been occurring for some time. The *onset* of inertial cavitation (and associated enhanced heating) should be detectable with a PCD well before a hyperechogenic region is observed on a B-scan. The implication is that if the clinician waits until hyperechogenicity is observed, one is already in an uncontrolled situation.

We tested this hypothesis in an Agar-graphite tissue phantom employing simultaneous B-Mode and PCD sensing. Figure 2.13 shows that inertial cavitation activity sets in at far lower pressures in these phantoms than can be detected via conventional ultrasound (0.9 MPa versus 1.5 MPa). This finding is important for two reasons. First, it indicates that cavitation in HIFU may go undetected if B-scans are the only diagnostic tool employed. Second, it points out the need for some type of sensitive detection scheme (such as PCD) to be able to detect, monitor, and control HIFU cavitation in vivo.

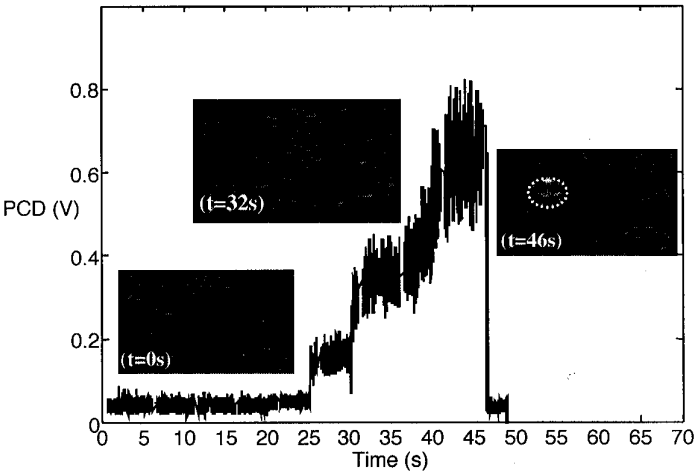

Figure 2.13. PCD output vs acoustic pressure during a ramp experiment (P was increased 0.15 MPa every 5 s). Selected ultrasound B-scan images are overlayed. At 46 s of continuous HIFU exposure and a peak negative focal pressure of 1.5 MPa a hyperechogenic region appeared on the B-scan image (inside dotted circle, at predicted focus indicated by gray cross).

2.2 Lesion migration

The shape of the thermal lesion resulting from HIFU exposure is qualitatively different when cavitation bubbles are present. A 'normal' thermal lesion (see, for example, Fig. 1.1) would be directly calculable from Eqs. (1-3), and would have an ellipsoidal shape. However, at relatively high intensities, many studies have shown that the resulting lesion shape has been described as a 'tadpole', having a larger lateral extent on the pre-focal side [64, 65,66,67]. Moreover, the shape and size are time-dependent, with the lesion growing towards the transducer and increasing in lateral extent the longer the insonation. Though many reasons have been set forth to explain such behavior, it is generally accepted that the presence of cavitation bubbles initially in the focal zone dramatically alters the propagation of the acoustic field. We will show modeling results in a later section which can elicit this behavior.

In order to have experimental results which we could compare to simulation, experiments were performed in optically transparent acrylamide gel phantoms containing a small amount of bovine serum albumin (BSA) whose denaturation upon heating mimics tissue death and lesion formation [68]. Figure 2.14 shows both a 'normal' lesion at modest pressure, and a 'tadpole' lesion at higher pressure.

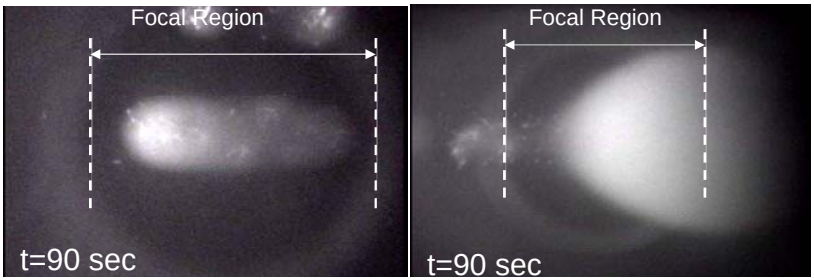

Figure 2.14. Controlled lesion (diffuse light area on gray background) at 3 MPa CW insonation for 90 seconds (left) and uncontrolled lesion at 5.5 MPa (right) in an acrylamide phantom containing 7% BSA by weight. 1 MHz HIFU is propagating from right to left. The dashed lines labeled "Focal Region" indicate the axial locations of the first minima surrounding the focal maximum (roughly -13 dB down from maximum) Note the change in optical magnification for each image.

2.3 Bubble migration

The tadpole-shaped lesions have their origin in the effect of bubbles on the acoustic field. If some or all of the focal zone becomes populated by cavitation bubbles, then the effective sound speed and attenuation will be dramatically altered, assuming the bubble sizes are mostly below the resonance size dictated by the primary HIFU field (for 1 MHz HIFU this means smaller than 1 micron radius). In a later section we will show that the shape instability threshold will, for modest effective viscosities, dictate that bubbles near or above resonant size will break up.

We wanted to visualize the bubbles created without the resulting lesion formation. To accomplish this we used acrylamide phantoms, but without BSA; the resulting molded gels are remarkably optically clear, very nearly index-matched to water. To the apparatus illustrated in Fig. 2.4, we added a video camera, with direct collimated broadband backlight. Figure 2.15 illustrates the development of the bubble field *within* the focal zone, before the inevitable growth into the prefocal zone. Time increases from left to right in the sequence (and the images are unevenly spaced in time). Each image is roughly the first half of the focal spot size, and the HIFU transducer is located to the left and out of the picture. The first image is just after the onset of cavitation, and several isolated regions of cavitation activity are visible as dark spots on the light background. In the second image, after a pressure increase of approximately 0.4 MPa above the first image, the growth of one of the initial cavitation zones back towards the HIFU transducer is visible (more dramatically seen in the video). Note the 'fingering' of the growth reminiscent of dendritic crystal growth and well known from bubble cloud studies [69]. The third and fourth images are at

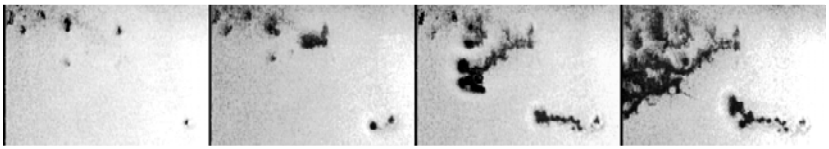

Figure 2.15. Series of 4 images depicting the growth of the cavitation zone. HIFU propagates from left to right in each image. The length of each image is roughly 1 cm, thus corresponding roughly to half of the focal zone. From left to right, time is increasing (in unequal increments). The pressure for each image is, from left to right, 1.7, 2.1, 2.1 and 2.1 MPa at 1.1 MHz. A processed gray scale is employed; bubbles appear dark on a light background.

the same pressure as the second image, only later in time (roughly 1-2 seconds have elapsed for images 2-4, a function of pressure above the threshold). The entire cavitation zone is now the length of the focal spot and increasing in axial and radial size as it moves back towards the transducer. This fingering is modeled in a subsequent section of the Chapter.

2.4 Duty cycle effects and control

The PCD can also indicate when shielding and uncontrolled "tadpole" lesion growth (as shown in Fig. 2.14) occurs. The PCD output becomes erratic, and its RMS value decreases for constant HIFU parameters when shielding occurs. Based on this result, we investigated varying both the pulse length and duty cycle. We find that certain combinations of pulse length and duty cycle can maintain and actually increase cavitation activity (at constant acoustic pressure) measured by the PCD for arbitrarily long insonations.

Figure 2.16 shows the PCD output vs time for a 2.1-MPa focal pressure HIFU insonation at 1.1 MHz for two cases, CW and CW followed by pulsed. As this is well above the threshold for cavitation, the PCD senses noise immediately after the HIFU is turned on, followed by a steadily decreasing noise level in the focal zone of the PCD (which, since the PCD was oriented at 90 degrees from the HIFU axis defines the central slice of the HIFU focal zone.) Both runs exhibit a sharp decrease in cavitation activity for the first 5 seconds during which time they are both CW. At 5 seconds, the drive signal was switched to a pulsed mode at 20% duty cycle for the second case. The CW case continues its precipitous decline, illustrating the shielding effect of uncontrolled cavitation. However, the pulsed case demonstrates both that pulsed HIFU can control cavitation, and that the PCD RMS signal is potentially a good feedback signal for active control.

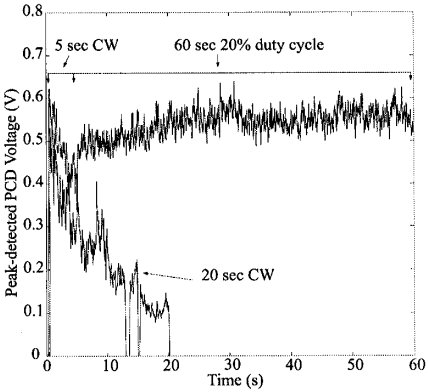

Figure 2.16: Peak PCD voltage vs time for a 1.1-MHz, 2.11-MPa HIFU insonation. The lower curve represents a CW insonation exhibiting the effects of shielding. The upper curve was CW for the first 5 seconds, then the HIFU was switched to pulsed mode (2.2 kHz PRF, 20% duty cycle) and continued beyond a minute with no degradation in cavitation activity.

3. Modeling results

Having seen the breadth of phenomena associated with bubble dynamics in HIFU, we now turn to a mathematical treatment of bubble dynamics (for a comprehensive overview of bubble dynamics see Leighton [70]). We seek to model the dominant physics, not all the physics, in an attempt to be able to reproduce the macroscopic results (enhanced heating, lesion migration, bubble fingering) we have presented in the experimental section of this Chapter. We note at the outset that our goal here is to apply well-known bubble dynamics theory in a unique way in order to provide both explanatory and predictive capabilities. We also note that this is necessarily an incomplete picture, that not only are results from other groups omitted (though we have tried to reference them) but also that this is still a work in progress.

A further note concerning the applicability of the models. The most important (some might say egregious) assumption we make is that the bubble dynamics can be modeled by treating the host medium (whether tissue or blood) as an effective Newtonian viscous fluid, where the effective shear viscosity is a parameter to be determined by a combination of experiment and modeling. Our primary justification for this assumption is that it allows us to calculate parameter dependences over large ranges of those parameters, without which we would be at a loss in trying to compare macroscopic HIFU experiments with single bubble dynamics results. Further justification is to be derived from the idea that relaxation

time scales for tissues are far longer than the time scales associated with the bubble dynamics. Finally, effects like shear thinning, while important in the 10-1000 Hz range, will not play a role for bubble dynamics, as the bubble dynamics will take place in the asymptotic limit of high strain rates.

3.1 Single bubble dynamics

3.1.1 Radial model

The radial equation of motion we use is the so-called Keller-Miksis equation [71,72]

$$\left(1-\frac{\dot{R}}{c_L}\right)R\ddot{R}+\frac{3}{2}\left(1-\frac{1}{3}\frac{\dot{R}}{c_L}\right)\dot{R}^2=\frac{1}{\rho}\left(1+\frac{\dot{R}}{c_L}+\frac{R}{c_L}\frac{d}{dt}\right)p_B - \frac{1}{\rho}\left(1+\frac{\dot{R}}{c_L}\right)\left(p_\infty - p_s\left(t+\frac{R}{c_L}\right)\right) \tag{6},$$

where dots denote time derivatives, R is the bubble radius, c_L is the sound speed in the surrounding medium, ρ is the density of surrounding medium, p_∞ is the ambient pressure, $p_s(t)$ is the applied acoustic field pressure and p_B is the pressure on the surrounding medium side of the interface between the medium and the bubble. p_B is related to the internal pressure p of bubble by the following formula:

$$p = p_B + \frac{2\sigma}{R} + 4\mu\frac{\dot{R}}{R} \tag{7},$$

where σ is the surface tension coefficient, and μ the shear dynamic viscosity. The sound field is sinusoidal:

$$p_s(t) = p_a \cos\omega t \tag{8},$$

with p_a the acoustic amplitude and ω the driving angular frequency. Most therapeutic applications of ultrasound rely on rather long tone bursts, approximating CW conditions. Our model is not limited to sinusoidal forcing, but experimental [26] and numerical [42] results show that with our experimental material parameters, sound fields in tissue and tissue-mimicking media are very weakly nonlinear, therefore the harmonics of ω are relatively unimportant for the bubble dynamics in the current application.

A model for the internal temperature and pressure of the bubble is described in detail in Prosperetti *et al.*, [73] and Kamath *et al.* [74]. This model accounts for heat transport by convection and conduction to and from

the surrounding medium. The model was derived by assuming an ideal gas and spatial uniformity of the gas pressure inside the bubble. The internal pressure p can be found by integrating:

$$\dot{p} = \frac{3}{R}\left[(\gamma - 1)K\frac{\partial T}{\partial r}\bigg|_R - \gamma p\dot{R}\right] \tag{9},$$

where γ is the ratio of the specific heats of the gas and K is the gas thermal conductivity. The gas temperature field $T(r,t)$ is obtained from

$$\frac{\gamma}{\gamma - 1}\frac{p}{T}\left(\frac{\partial T}{\partial t} + \upsilon\frac{\partial T}{\partial r}\right) = \dot{p} + \frac{1}{r^2}\frac{\partial}{\partial r}\left(\kappa r^2\frac{\partial T}{\partial r}\right) \tag{10},$$

with

$$\upsilon = \frac{1}{\gamma p}\left[(\gamma - 1)K\frac{\partial T}{\partial r} - \frac{1}{3}r\dot{p}\right] \tag{11},$$

where υ is the radial velocity of the gas inside of the bubble. The temperature boundary condition for a relatively cold liquid, such as water at normal ambient temperature, is,

$$T\left[r = R(t), t\right] = T_\infty, \tag{12},$$

where T_∞ is the undisturbed liquid temperature.

The solution of this set of equations of motion (6)-(12) requires numerical integration. Kamath and Prosperetti developed a Galerkin spectral method of solution which we employ in this work. For more detail the reader is referred to [43].

Figure 3.1 gives the reader an overview of the radial or breathing mode response as a function of both bubble size and host medium viscosity for a typical pressure of 1 MPa at 1 MHz. The expansion ratio plot (top), which also predicts inertial cavitation, has a sharp maximum (referred to[75] as a "giant resonance") on the order of 100 for small (100 nm) bubbles at low (0.001 – 0.01 Pa-s) viscosities. The maximum radius exhibits several resonance peaks for micron-sized bubbles, and shows a broad and nearly flat plateau for bubbles from 100-1000 nm. In both plots the Blake threshold is clearly seen below 100 nm for the lowest viscosities. These typical features of radial bubble dynamics will govern the quantities derived from the response which we present in the next few sections.

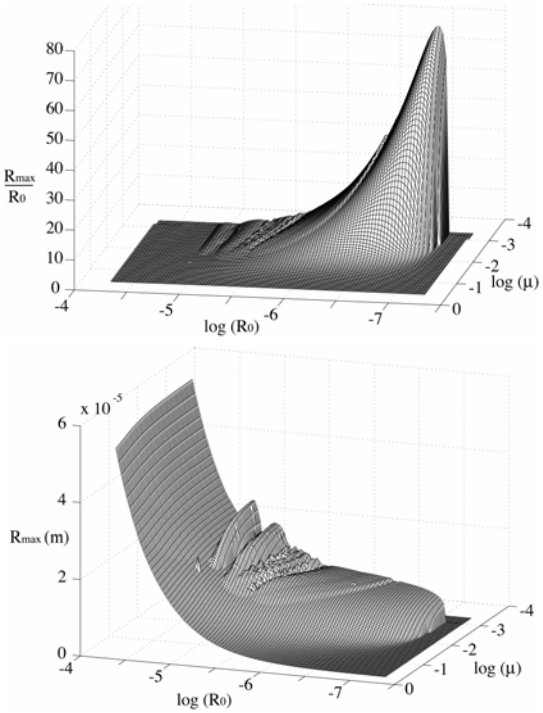

Figure 3.1. Cycle-averaged maximum radius (bottom) and expansion ratio (top) for a single bubble (Eq. 6) driven with 1MPa, 1MHz sinusoidal input. The reference values are 1 micron for R_0 and 0.001 Pa-s for μ.

3.1.2 Heat deposition

The conversion of the bubble's mechanical energy into thermal energy constitutes the dominant pathway for enhanced heating during HIFU treatment. A discussion of several mechanisms may be found in [26,76,77,78]. Here we use a single-bubble model and focus on the two dominant damping mechanisms [79,80]. We assume that the bubble concentration is sparse so that bubble interactions can be ignored.

Power deposition through viscous dissipation at the bubble wall is obtained from the product of the viscous force and the bubble wall velocity [80]:

$$W_{vis} = 16\pi\mu R\dot{R}^2 \tag{13}.$$

This energy is dissipated solely as heat in the medium; and therefore this term is identically the viscous heating contribution. Figure 3.2 shows the

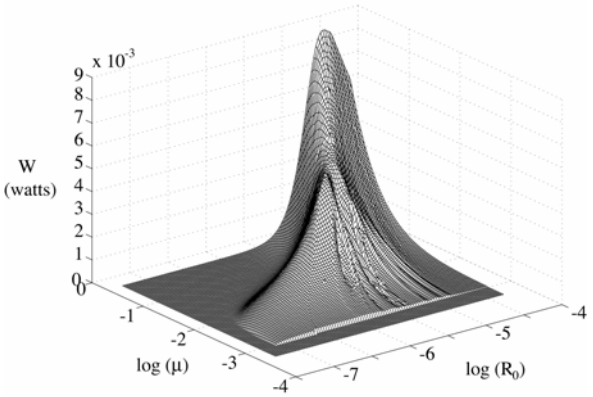

Figure 3.2. Cycle-averaged thermal power generated by the viscous heating mechanism (Eq. 13)

thermal power generated by a single bubble as a function of bubble size and medium shear viscosity. A broad maximal ridge exists along a diagonal for bubbles larger than the resonant size and viscosities larger than 10 times water. The peak power is roughly 10 mW.

Acoustic emission from an oscillating bubble consists of two parts: 1) the passive emission; 2) the active emission. The passive emission is due to the presence of the object in the primary HIFU field, and is negligibly small for micron- and submicron-sized bubbles. The active emission radiated by the strongly nonlinearly oscillating bubble will be (by orders of magnitude) the dominant term. The acoustic emission from a volume oscillator has the following form,

$$p_{sac}(r,t) = \frac{\rho}{4\pi r}\frac{d^2V}{dt^2}, \tag{14}$$

where r is the radial distance from the oscillator and V is the volume of the oscillator. At a distance r, the total emitted sound power is

$$W_{sac} = 4\pi r^2 I = \frac{4\pi r^2}{\rho c}\int_0^{+\infty} p^2{}_{sac}(t)dt = \frac{4\pi r^2}{\rho c}\int_{-\infty}^{+\infty} p^2{}_{sac}(f)df, \tag{15}$$

where $p_{sac}(f)$ is the Fourier transform of $p_{sac}(t)$. This formulation [76] allows a frequency-dependent absorption law to be used. If at the bubble surface the

emitted sound power is W_0, then the power deposition in the volume bounded by r is W_0-W_{sac}.

Figure 3.3 shows the thermal power resulting from the absorption of the bubbles acoustic emissions. The peaks in the power correlate well with the features in the expansion ratio graph in Fig. 3.1. Absolute size dominates for bubble sizes much greater than resonant, but these bubbles will be seen in the next sections to be 'forbidden', either shape unstable or dissolving.

Figure 3.4 plots the thermal power for the same parameter space but for a higher pressure of 2.8 MPa. These results indicate that the power developed by the secondary acoustic emission mechanism is on the order of 50 mW for much of the parameter space investigated, while the viscous mechanism achieves comparable powers only for the largest viscosities considered.

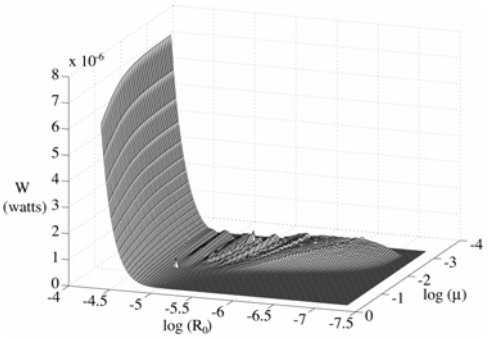

Figure 3.3. Cycle-averaged thermal power generated by the absorption of the secondary acoustic emissions from collapsing bubbles (Eq. 16) for a single bubble driven at 1 MPa and 1 MHz.

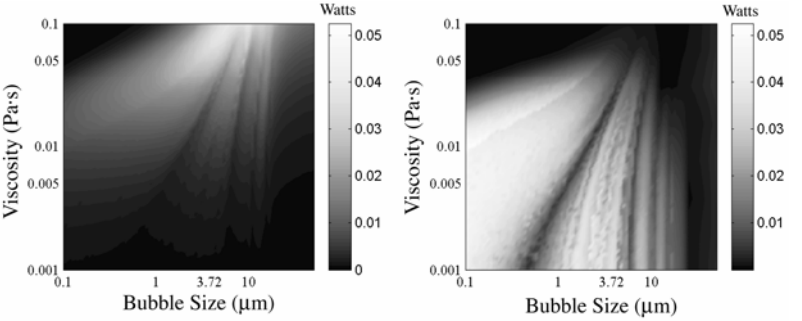

Figure 3.4. Single bubble heating contributions for a 1MHz, 2.8 MPa acoustic pressure. Viscous power (left) and secondary acoustic absorption power (right) are plotted vs bubble size and phantom viscosity.

If we choose 'optimal' bubble sizes for each type of contribution, then the optimal viscous source bubble would be roughly 4 μm at 0.07 Pa-s viscosity. The optimal secondary acoustic or inertial bubble would be say 200 nm at 0.003 Pa-s. We can then define the source strengths $q^*_{vis,rad}$ in Eq. (1) as $Nq_{vis,rad}$, where N is the number of bubbles in the focal region required to make up the difference between the primary acoustic heating and the bubble-enhanced heating observed in a situation as depicted in Fig. 1.2. Table 1 illustrates the results of such a calculation for a typical run:

Table 1. Number of bubbles required to achieve experimentally observed ΔT

Acoustic Pressure (MPa)	Experiment ΔT (°C)	Number of optimal viscous bubbles	Number of optimal inertial bubbles
2.06	6.8	10	10
2.18	8	12	12
2.30	10	16	15
2.41	12	17	16
2.53	15	22	22
2.64	21	27	28
2.76	24	35	35

It is rather striking that no more than 35 'optimal' bubbles would be required to generate an extra 24°C temperature rise. Certainly 35 is not to be taken exactly, but the order of magnitude is correct. Converted into a bubble number density by using the volume of space for which the acoustic pressure (without including bubbly propagation effects) is above the detectable cavitation threshold for these phantoms (roughly 1.5 MPa) yields on the order of 10 mm^{-3}, increasing as the pressure increases above the threshold.

3.1.3 Shape instability

Even in optically clear media, quantifying a bubble size distribution experimentally is difficult [52]. The difficulties are compounded when working with tissue or opaque tissue-mimicking phantoms. We therefore turn to an investigation of the stability of bubbles in hopes of gaining some insight into the size range of bubbles which could contribute to HIFU effects. We begin with the spherical shape. An instability to wavy surface perturbations will cause shape oscillations of a spherical bubble [81,82,83,84,85]. Consider a small axisymmetric distortion of the spherical interface $R(t)$,

$$r = R(t) + a_n(t)P_n(\theta) \tag{16}$$

where P_n is the Legendre polynomial of degree n, $a_n(t)$ is the amplitude. The shape distortion consists of a superposition of modal surface oscillations whose

amplitudes are given by $a_n(t)$. The problem is to determine how the $a_n(t)$ behave, and which modes contribute.

Experimental observations [86,87] of the onset of shape instability for a bubble in water show quantitative agreement with predictions [85,88] regarding mode n observed and dependence on bubble size for all models of bubble oscillation. For the radial model Eq. (6-12), and with the following approximations (17) – (20), good quantitative agreement can be expected in the single bubble sonoluminescence range, corresponding to inertially collapsing bubbles where the driving frequency is around 20 kHz and driving pressure is 0.8-1.4 atm.

The equation governing the time evolution of the $a_n(t)$ is;

$$\ddot{a}_n + B_n(t)\dot{a}_n - A_n(t)a_n = 0 \tag{17}$$

with

$$A_n(t) = (n-1)\frac{\ddot{R}}{R} - \frac{\beta_n \sigma}{\rho R^3} + \frac{2\nu\dot{R}}{R^3}\left[-\beta_n + n(n+2)(n-1)\frac{1}{1+2\delta/R}\right] \tag{18}$$

$$B_n(t) = \frac{3\dot{R}}{R} + \frac{2\nu}{R^2}\left[-\beta_n + \frac{n(n+2)^2}{1+2\delta/R}\right] \tag{19}$$

where $\beta_n = (n-1)(n+1)(n+2)$, ν is the kinematic viscosity, a_n is the amplitude of the n-th surface mode, and the boundary layer thickness δ is approximated by

$$\delta = \min\left(\sqrt{\frac{\nu}{\omega}}, \frac{R}{2n}\right) \tag{20}$$

$R(t)$ is obtained from the numerical solution of the equation of motion (6). The ordinary differential equation (17) can then be solved numerically using numerical values of R, $\dot{R}$, and $\ddot{R}$ from (6).

A suitable method for investigating parametric instability for periodic solutions is Floquet analysis [89]. Parametric instability occurs whenever the magnitude of the maximal eigenvalue of the Floquet transition matrix $F_n(t)$ of Equation (9) is larger than one. The Floquet transition matrix is defined by

$$\begin{pmatrix} a_n(T_p) \\ \dot{a}_n(T_p) \end{pmatrix} = F_n(T_p)\begin{pmatrix} a_n(0) \\ \dot{a}_n(0) \end{pmatrix} \tag{21}$$

where T_p is the period of the response (which does not have to be the period of the acoustic field). Figure 3.5 illustrates periodic radial oscillations unstable to perturbations of the quadrupole (n=2) mode.

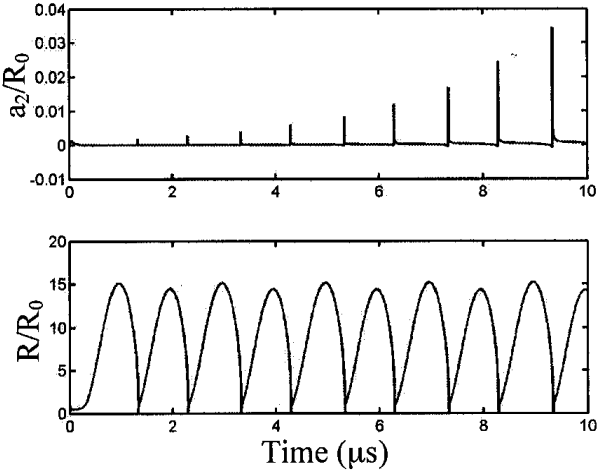

Figure 3.5. Spherical radius *R(t)* and n=2 shape mode amplitude $a_2(t)$ for periodically oscillating subresonant bubble. P=2.0MPa at 1MHz. R_0=1μm and μ=0.01N·s/m^2.

Floquet analysis fails for chaotic oscillations of the bubble radial motion [90,91]. The chaotic range (for bubbles at the onset of shape instability) extends from about 2 μm to more than 20 μm for viscosities from 0.001 to 0.02 Pa-s at 1 MHz, at the pressure range of 1 MPa - 3 MPa. In the chaotic region, a small fluctuation (<1 nm) is given as the initial distortion, and the following approximation criterion is used for breakup via shape instability:

$$\max\left(\frac{|a_n(t)|}{R(t)}\right) \geq 1 \tag{22}$$

Note that Eq. (22) is a valid criterion for breakup for any type of motion, as long as a sufficient number of modes n are investigated. We solve the *R(t)* curves for as many cycles as it takes to reach steady state, and observe the $a_n(t)$ curves. Note our results account for both Rayleigh-Taylor instability (governed by the $\ddot{R}$ term in A_n in Eq. (18)) and parametric instability (governed by the $\dot{R}$ term in B_n in Eq. (19)) for any practical time scale. Fig. 3.6 illustrates an unstable n=2 mode during a chaotic radial oscillation.

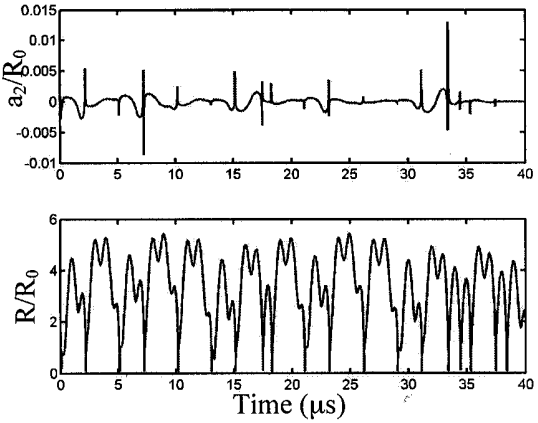

Figure 3.6. Spherical radius *R(t)* and n=2 shape mode amplitude $a_2(t)$ for chaotically oscillating subresonant bubble. P=2.0MPa at 1MHz. R_0=4μm and μ=0.06N·s/m^2.

The above methods worked well for subresonant bubbles, and for resonant bubbles, whose size range extended to approximately 20 microns for the pressures investigated. For bubbles larger than resonant size, it became computationally impractical to compute higher and higher shape mode orders n to determine which was dominant. For these "superresonant" bubbles, we assume the Faraday instability [92,93] dominates the shape instability. The most unstable mode can be chosen as follows: We calculate the inviscid shape mode frequency for each Legendre mode, which is given by Lamb [94] as $\omega_n = (n-1)(n+1)(n+2)\frac{\sigma}{\rho R_0^3}$. The most unstable mode should have a mode frequency which is exactly one-half of the driving frequency, ($\omega_n = \omega_0/2$ = 500 kHz) as required by the linearized Faraday parametric instability. After finding the threshold Eq. (22) for the chosen mode at this value of R_0, we then numerically investigate several nearby modes to determine the highest threshold value of viscosity for a given R_0. We finally choose the largest critical value of viscosity as the threshold point. The critical values of the most unstable modes for all R_0 comprise the boundary of bubble shape instability for superresonant bubbles. Figure 3.7 plots the threshold for shape stability for superresonant bubbles for a variety of pressures. The power-law scaling follows from linear bubble dynamics. Combining all 3 shape instability calculations for a given pressure will yield regions of stable, allowed bubbles in the viscosity and size parameter space – these are best viewed on the same plot (below) with the rectified diffusion thresholds from the next section.

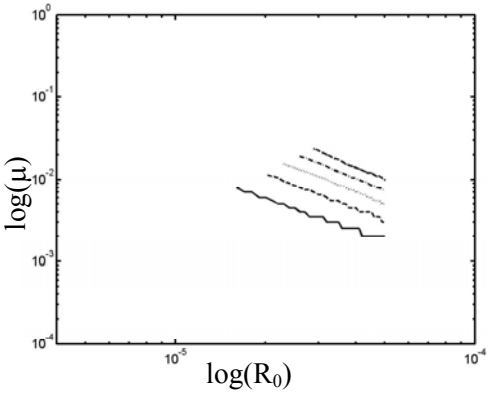

Figure 3.7. Bubble shape instability thresholds for superresonant bubbles. These threshold lines correspond to driving pressures of 1.0 MPa, 1.5 MPa, 2.0 MPa, 2.5 MPa, and 3.0 MPa from bottom to top line respectively. At a given pressure, bubbles below the threshold line are shape unstable, while those above the threshold remain spherical. $\mu = 1$ N·s/m^2 and $R_0 = 1$ m.

3.1.4 Rectified diffusion

A static bubble will dissolve unless stabilized by some mechanism (encapsulation, for instance). An oscillating bubble will dissolve, stay the same size (the least probable outcome) or (the most likely outcome for HIFU) grow by rectified diffusion [95,96,97]. The time-average growth is given by [98,99]

$$\frac{dR_0}{dt} = R_0\omega_0 \frac{R_g T_\infty \rho}{M p_\infty} \frac{1}{Pe}\left(1+\frac{4\sigma}{3R_0 p_\infty}\right)^{-1} \frac{\left(c_i - c_0\left\langle p_G^*(\tau)\right\rangle_{\hat{\tau}}\right)}{\int_0^\infty \frac{dU}{\left\langle\left(3U + x^3(\tau)\right)^{4/3}\right\rangle_{\hat{\tau}}}} \tag{23}$$

where R_g is the universal gas constant, R_0 is the equilibrium radius of bubble, T_∞ is the temperature of the surrounding liquid, ρ the density of liquid, M the molecule weight of gas inside the bubble, p_∞ the ambient pressure, P_e the *Péclet* number, σ the surface tension, and c_0 the saturation concentration in the liquid. The validity of this method depends on the *Péclet* number being large, which can be easily satisfied in most cases. The rectified diffusion threshold is given when the growth rate is zero,

$$c_i - c_0\left\langle p_G^*(\tau)\right\rangle_{\hat{\tau}} = 0\,, \tag{24}$$

Figure 3.8 plots the growth rate as a function of bubble size and medium viscosity. Dramatic growth occurs coincident with the large peak in the expansion ratio seen in Fig. 3.1.

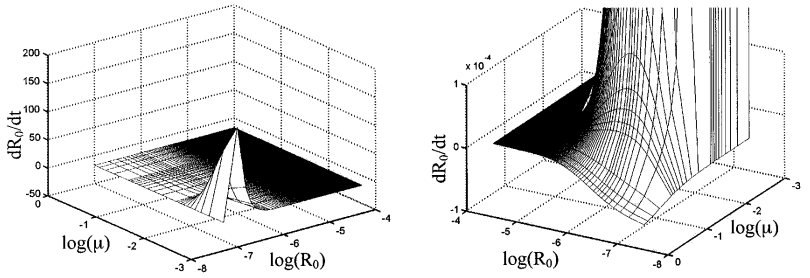

Figure 3.8. Bubble growth rate (Eq. (23)) at 1 MPa, 1 MHz and dissolved gas concentration 100%. The right plot shows details by zooming in a region of the plot on the left. Note the rotation of the coordinate system from left to right plot.

3.1.5 Predicting the bubble size distribution

Only bubbles that do not dissolve and that are shape stable will contribute to the heating. Bubbles which contribute to heat generation will thus be trapped in the wedge-shaped region between the two instability thresholds, as shown in Fig. 3.9. Additionally in Fig. 3.9 we have indicated the threshold for inertial cavitation (defined by the minimal criterion of expansion ratio ≥ 2), since our experiments show that inertial cavitation as detected by the PCD correlates with bubble enhanced heating.

The resulting bubble size distribution is thus seen to depend (for a given pressure and dissolved gas concentration) on the medium viscosity. The smallest bubble size is defined by the threshold for growth by rectified diffusion (the nearly vertical part of RD100 on the left side of the plot) – bubbles smaller than this threshold cannot expand sufficiently and will dissolve. Since this boundary is coincident with the sharp rise in expansion ratio seen in Fig. 3.1, we may refer to this lower boundary as the Blake threshold. For water-like viscosities and essentially any dissolved gas concentration, bubbles above the Blake threshold will rapidly grow until they encounter the shape instability threshold, where they will break up, and one or more fragments will repeat the process, potentially increasing the number of bubbles. The size range for such bubbles is between 10 nm and roughly 1 micron.

In contrast, for viscosities greater than about 20 times water, bubbles above the Blake threshold will grow slowly until they again encounter the

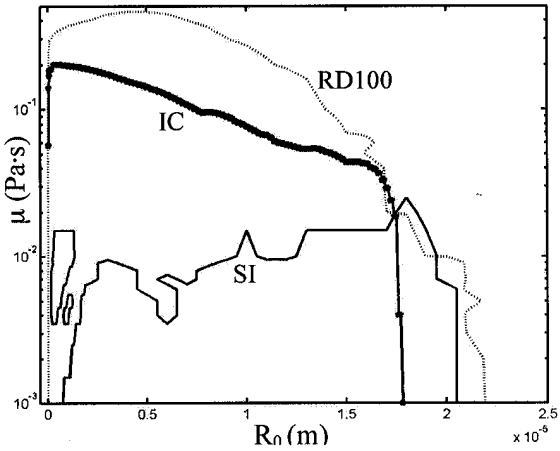

Figure 3.9. P_a=2.5 MPa, f=1 MHz and 100% gas saturation. Rectified diffusion (RD100, dashed line), shape instability (SI, thin solid line) and inertial cavitation (IC, thick solid line with stars) thresholds at P_a=1 MPa, f=1 MHz. Below RD bubbles grow. Below IC bubbles collapse inertially. Below and enclosed by SI bubbles break up from shape instabilities.

rectified diffusion threshold, where they may remain since this represents a stable equilibrium. The upper bound will change depending on the dissolved gas concentration. To cite two extreme cases, for 0.1% saturation (not shown), the bubble size distribution will range from about 10 nm to only 2 microns. For 100% saturation (shown as RD100), bubbles grow as large as 18 microns, many times the (linear) resonant size.

3.1.6 Temperature effects

As the HIFU focal zone temperature increases there will be increasingly strong effects on the bubble dynamics, mostly owing to the changes in material properties as a function of temperature. Though there have been several studies of acoustic properties of tissue as functions of temperature, there are no available studies of the mechanical properties which will be more important for bubble dynamics. Since the primary constituent is water, and since also cellular matter (membranes, etc…) will be increasingly fragmented as bubble activity continues, we have chosen the temperature dependence of water to model the effects of increasing temperature on HIFU bubble dynamics.

The primary properties which will affect the bubble dynamics are: surface tension, which will decrease to zero at boiling; viscosity, which will also decrease to zero at boiling; vapor pressure, which will increase to ambient pressure at boiling. The viscosity and vapor pressure will have direct effects on

the rectified diffusion and shape instability thresholds, resulting in smaller allowed bubble sizes. However, the most dramatic effects are in the radial response. Figure 3.10 shows the change in expansion ratio and in heat deposition for a single bubble as functions of ambient host temperature. While the models break down near boiling, the trend is clear. The expansion ratio decreases dramatically, and as a direct consequence bubbles acoustic emissions (and thus their detectability via PCD) decreases as well. Primarily because of the drop in expansion ratio, the bubble's thermal power deposition also decreases. Thus violently nonlinear bubble oscillations at low ambient temperatures change to modest and even linear oscillations at high temperatures. Bubbles will cease to be thermal sources or noise sources of any significance – however, they will continue to play a leading role in changing the acoustic propagation as shown in the sections below.

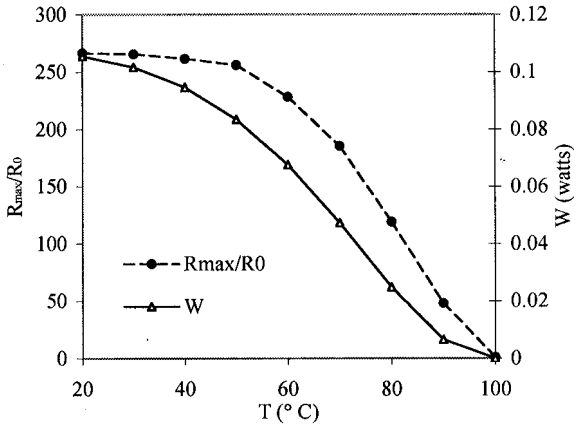

Figure 3.10. Bubble expansion ratio and thermal power as a function of ambient temperature for P_a=2.0 MPa, f=1 MHz. The plot was generated using the thermal properties of water.

3.2 Bubble zone dynamics

3.2.1 Bubble-tracking model for bubble zone development within the focal zone

The development of the bubbly zone as depicted in Fig. 2.15 is of considerable interest. If the development could be modeled, then all the resulting effects (heat deposition, noise emission, effective medium properties) could then be calculated in a straightforward manner. What is required, however, is a knowledge of the spatio-temporal dynamics of each bubble in the zone, as well as the time and space-resolved nucleation events. Nucleation is,

however, inherently non-deterministic – thus at the outset we can only know a bubble zone in a statistical sense. Nevertheless such a statistical sense should, suitably averaged, be able to predict the necessary macroscopic properties.

We attempt to model the development of the bubble zone by removing time explicitly from the problem – the justification is both practical (we cannot run the bubble and propagation codes with 100 micron resolution and acoustic time scales for durations of seconds) and necessary (we cannot predict when a nucleation event will occur). Therefore we choose an iterative scheme in which medium properties are updated by resetting each element in the propagation code. The computation (illustrated in Fig. 3.11) proceeds thusly: We run the propagation codes for an initially homogeneous material with a single nucleation site within the focal zone, which is computed on a 100 micron x 100 micron grid. The pressure field is calculated for each 'pixel' (recall this is a 2D computation). If the pixel pressure exceeds the empirically defined nucleation threshold P_{th} (which we take to be our experimentally determined inertial cavitation threshold for our phantoms) then we initiate a random number generator to yield a nucleation likelihood estimator γ between 0 and 1. This estimator is then compared with two independent normalized 'thresholds' associated with two mechanisms of nucleation: pre-existing nuclei γ_p, and collapse-generated nuclei γ_c. Both are normalized between 0 and 1. γ_p indicates the threshold for nucleation at any location once $P > P_{th}$ owing to pre-existing nuclei. Thus, for example, we would choose γ_p relatively low if the host medium were an agar-graphite phantom saturated with gas, but high if the host medium were in vivo with no added agents. γ_c represents the threshold for the medium to nucleate from a fragment or weakening owing to nearby cavitation activity. γ_c would be low if the host viscosity were low and the eventual fate of most bubbles was breakup via shape instability, but high if the viscosity were high and bubbles could remain stable. Additionally, γ_c is initially set high for every pixel, and is only lowered if the pixel is a nearest neighbor of a cavitation site. If either $\gamma > \gamma_p$ or $\gamma > \gamma_c$, the pixel is a cavitation site: R_0 is determined from the ambient and driving conditions using data like that in Fig. 3.9, and the bubble dynamics equations are run. Then a new attenuation and sound speed for that pixel are recalculated based on the bubble dynamics, discussed in the next section. Once all such cavitation site pixels are calculated, the sound propagation equations are run again, and the process repeats itself.

Figure 3.12 illustrates 2 results from our computations representing 2 extreme cases. The first case simulates the condition of plentiful preexisting nuclei in the host medium (γ_p low); the lower graph simulates the condition of sparse preexisting nuclei, where most cavitation is generated from existing cavitation. Only the endpoints of 100 iterations are shown, and it is

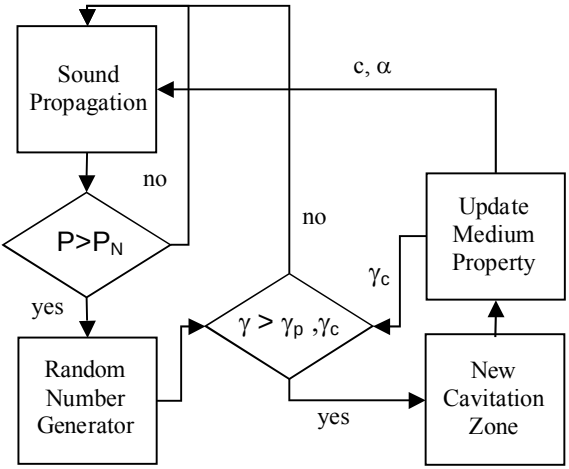

Figure 3.11. Flowchart for predicting development of cavitation zone.

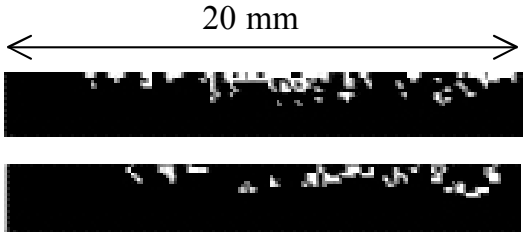

Figure 3.12. Simulations of developed cavitation zone from a 1 MHz HIFU focused bowl transducer (not shown) propagating from left to right. Only the lower half space is calculated. Top is plentiful preexisting nuclei, bottom is sparse nuclei.

not definitively clear from viewing these endpoints alone that the sparse case represents our data better than the plentiful case. It is more evident when the iterative development of the cavitation zone is viewed. Nevertheless the connectivity of cavitation sites seen in the experiment is more faithfully captured in the simulation where the dominant nucleation mechanism is 'seeding' from existing cavitation sites. This microscopic approach has one or two disadvantages. First, it is computationally intensive and cannot run in real time, and even so we have not included such potentially important effects as bubble-bubble interactions. Second, the bubble's effect on the sound field is that of a scattering site of 100 micron on edge – clearly a cumbersome approximation. We turn next to a bubble dynamics-based effective medium approach.

3.2.2 Effective medium model

We take an effective medium approach here, assuming that some appropriate subset [42] of the HIFU focal (or near-focal) region may be treated as a classical effective continuous medium. The presence of a bubble population in a sound field will cause a change of the effective attenuation and sound speed in the focal zone, which we then incorporate into the propagation Equation (1). The effective absorption coefficient can be evaluated through the calculation of the extinction cross section [70],

$$\sigma_{ext} = \frac{W_{ext}}{I_{inc}} \tag{25},$$

where W_{ext} is the power loss from both radiation and viscous damping at the bubble surface, calculated numerically from the full nonlinear bubble dynamics in Eqs. 13 - 15. A plane wave of intensity I_{inc}, traveling a distance Δz through a population of N_b bubbles per unit volume, each having an extinction cross section σ_{ext}, has its intensity reduced by $\Delta I = -N_b \sigma_{ext} \Delta z$. Then integration gives

$$I = I_0 \exp\left(-N_b \sigma_{ext} z\right) \tag{26},$$

where I_0 is the intensity at z=0. Thus the (pressure) attenuation for the effective medium $\alpha_{eff} = N_b \sigma_{ext}/2$, a time dependent function.

The effective sound speed depends on both the effective gas volume fraction and the bubble response. From our studies of bubble response above, we know that HIFU allows bubbles whose size ranges from well below the linear resonance to above it, with a corresponding response of extremely nonlinear for bubbles below and of resonance size, to linear for bubbles larger than resonance size. For 'small' bubbles (which we operationally define as bubbles whose expansion is essentially in phase with the rarefaction phase of the local acoustic pressure) we use Wood's equation to predict the sound speed, which has the following form [100]

$$\frac{1}{c_{mlf}^2} = \frac{(1-\chi)^2}{c_l^2} + \frac{\chi^2}{c_g^2} + \chi(1-\chi)\frac{\rho_g^2 c_g^2 + \rho_l^2 c_l^2}{\rho_l \rho_g c_l^2 c_l^2} \tag{27},$$

Where c_l is the sound speed in liquid, c_g is the sound speed in gas, ρ_l and ρ_g are the density of the liquid and gas respectively, χ is the gas volume fraction and c_{mlf} is the effective medium sound speed in the mixture, where 'lf' means 'low frequency'. In classical linear approximations low frequency is taken to mean well below the bubble's linear frequency, which one can see corresponds with

our nonlinear notion of in-phase expansion. Since we deal with strongly nonlinear bubbles, the gas volume fraction χ is computed using a time-average bubble volume,

$$V_{gas} = \left\langle \frac{4}{3}\pi R(t)^3 \right\rangle_t \tag{28}.$$

One can appreciate that for bubbles whose expansion ratio is of the order of 100 this formulation will yield a dynamic gas volume fraction which exceeds the static fraction by a factor of 10 – 100. Note also that such a formulation yields an *implicitly dispersive* medium – the effective sound speed will be a function of frequency (and sound amplitude as well) by virtue of the change in the bubble dynamics and bubble size distributions.

For bubbles larger than the resonance size and which behave linearly, we may employ the more traditional resonance addition to the sound speed calculation, adopting the approach of Commander and Prosperetti [101], which yields an explicit expression for the wavenumber and thus sound speed (or phase velocity) with an explicit, rather than implicit dispersion relation.

The resulting attenuation coefficients and sound speeds for a bubble density of 1 mm^{-3} are shown in Fig. 3.13. Three types of bubble populations (consistent with the stability diagram of Fig. 3.9) are selected. Type I (0.002 Pa-s, 1 micron) are subresonant bubbles with low viscosity, and their time series (not shown) for this pressure range is mostly chaotic. Type II (0.05 Pa-s, 2 micron) are near resonant bubbles with a viscosity 50 times that of water, whose time series exhibit periodic but nonlinear behavior. Type III (0.05 Pa-s, 15 microns) are superresonant bubbles existing at the same effective viscosity as Type II bubbles, and whose time series is also periodic and nearly linear. Note that the major qualitative difference is between subresonant bubbles and superresonant bubbles: the sound speed for the latter is essentially constant, whereas for the small bubble cases the sound speed is much less than the liquid sound speed. Moreover, the sound speed continues to decrease as the pressure increases, the result of the nonlinear oscillations resulting in ever larger effective void fractions in Eq. (28).

To illustrate the utility of this approach, a flow chart is presented in Fig. 3.14 illustrating how the prediction of a HIFU lesion proceeds. We choose a source pressure which would yield (in the absence of cavitation activity) a target focal pressure in normally absorbing tissue. That focal pressure is then used to run the bubble dynamics equations for a choice of input bubble size and effective medium viscosity. In what follows we will consider the three cases already introduced as Types I-III.

The bubble equations allow the calculation of an effective sound speed and attenuation coefficient, which is applied to the computational grid in the

'tissue' only for those grid points where the pressure is greater than the (experimentally determined) cavitation threshold. The acoustic wave equation is updated with the new spatial distribution of material parameters and run to calculate a new pressure distribution. This pressure distribution then defines a new primary heat source density, which is input to the heat conduction equation. The heat conduction equation then yields the spatial temperature distribution, from which a thermal dose is calculated.

The new pressure and temperature distributions are then used to calculate new bubble dynamics for the spatial regions where the pressure and temperature have changed since the last calculation. These iterations are repeated every 100 ms.

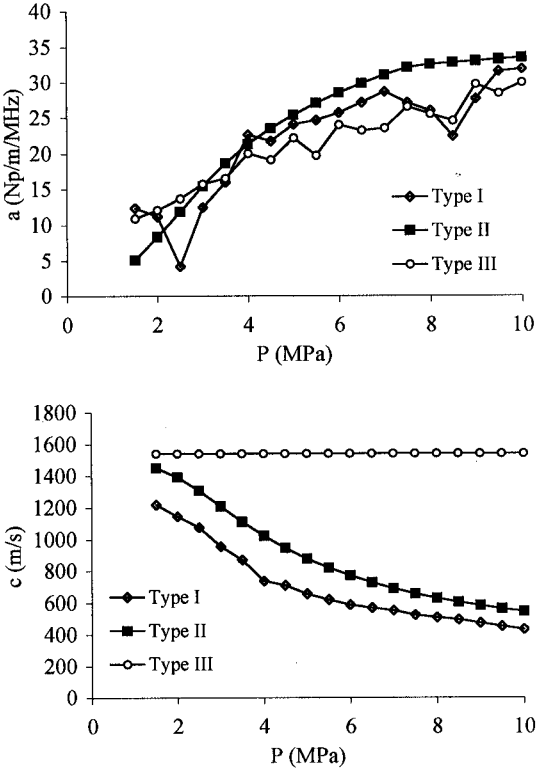

Figure 3.13. Effective medium attenuation coefficient (top) and sound speed (bottom) vs acoustic pressure for 3 effective viscosities and their corresponding allowed bubble size, calculated for a bubble number density of 1 mm^{-3}. Types I, II and III bubble parameters are discussed in the text.

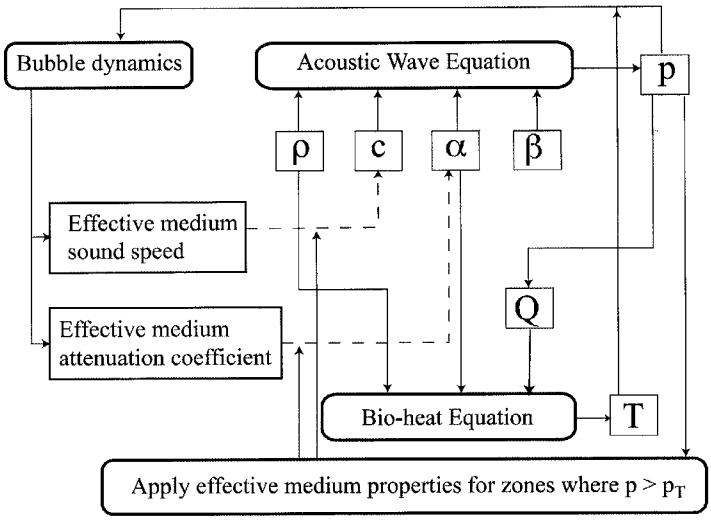

Figure 3.14. Schematic of the iteration process for computing the pressure, temperature and cavitation fields given a source pressure radiating from a transducer.

Figure 3.15 shows the resulting thermal lesion (defined as a dose equivalent to 240 minutes at 43 degrees) every second for each of the three types of bubbles defined earlier. One common feature illustrated by the results is the bubble-enhanced heating. Without bubbles (a case not shown), there is no region for which the thermal dose is above the 240min iso-dose contour for a 2 MPa, 10 sec CW HIFU treatment. With bubbles and bubble-enhanced heating present, however, zones with thermal dose above 240min emerge approximately 2 seconds after firing. There is a striking difference in the lesion shape and position depending on whether there are subresonant bubbles (Type I, left) or superresonant bubbles (Type III, right) in the focal zone. The Type I lesion migrates towards the transducer and appears to be tadpole-shaped. The Type III lesion grows more regularly around the focus, while the Type II lesion is intermediate. The attenuations of sub- and superresonant media are similar (Fig. 3.13) but the sound speeds are significantly different, inviting the conclusion that the sound speed change is the dominant mechanism for lesion distortion. The subresonant lesions match experimental observations of asymmetrical widening of the lesion in the prefocal area (see Fig. 2.14, note that there HIFU propagates from the right). Such results add even more evidence in support of the hypothesis that this Type I range of bubble sizes is mostly likely to be self-selected by the nonlinear interaction of HIFU and tissues.

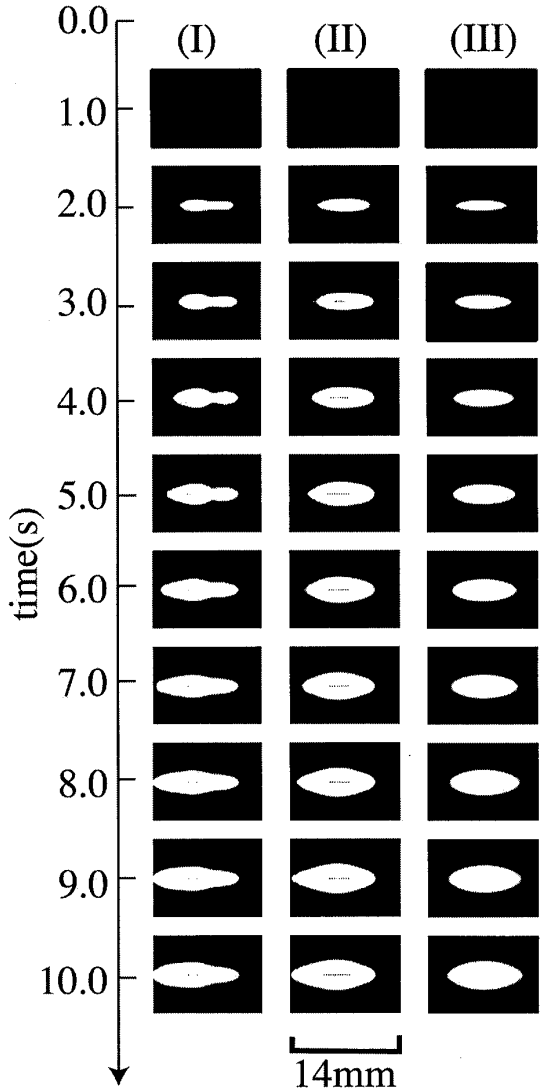

Figure 3.15. Thermal lesion development (white values indicate a thermal dose in excess of the threshold defined in the text) plotted at one second intervals from top to bottom. Results are shown for Type I (left), Type II (middle), and Type III (right) bubbles for a 5 second CW HIFU burst propagating from the left at 2 MPa and 1 MHz

for a bubble number density of 5 mm^{-3}. Types I, II and III bubble parameters are discussed in the text.

4. Looking forward

An important consideration when attempting to model any physical phenomenon is accuracy in the face of complexity. One must assess how much fidelity is required to capture the essential physical processes in light of how much *a priori* information is needed to inform the calculation or simulation. This is particularly relevant to the modeling of physical processes in biological media, where often much is unknown about the system. In looking forward to the future role of cavitation in therapeutic ultrasound, one is reminded that there is much that we simply do not know:

What is the dynamic viscosity of tissues at biomedical frequencies. Is it even possible to model tissue as a Newtonian medium given the strain rates encountered?

What is the surface tension of tissues?

What are the number densities of bubbles in cavitating fields, and how to they vary from one tissue type to the next?

Do cavitation nuclei exist in tissue and, if so, what is their nature?

Until we can answer these (and other) questions, the application of complex bubble and bubble field models to predicting cavitation-related outcomes *in vivo* is, at best, an exercise in guidance, not prediction. It is possible to use models to test hypotheses and interpret experimental results, but a detailed forward model that can unambiguously predict cavitation dynamics *in vivo* and accurately inform treatment planning eludes the community. This is an important technology barrier to be addressed as we move forward.

Ockham's 'razor', often stated as "*plurality should not be assumed without necessity*," encourages us to choose the simplest model possible that recovers the essential physical characteristics of a system under study. In doing so, one is frequently forced to adopt assumptions that serve to reduce the number of input parameters. Modeling a complex tissue as a Newtonian fluid with a fixed shear viscosity is one such example of "shaving off" complexity to achieve simplicity. The key question is: how much can one simplify the problem before a model loses its predictive capacity? Understanding which parameters and effects are really important and which can be approximated – or even ignored – will be a key facet of ongoing work in this field.

Predicting bubble dynamics and related physical effects is only one facet of the work reported herein. Bubble-enhanced ultrasound therapy is increasingly enabled by technology that allows us to monitor cavitation activity and heating in real time, either through acoustic scattering or noise diagnostics. This information can serve to inform the therapist (or therapy system) on the state of the bubble field in both space and time. Such information can be used to

then modify treatment parameters in order to attain or maintain a desired therapeutic condition. The interpretation of sensor data requires that we understand (or model) the relationship between the bubble field characteristics and the sensor output. Moreover, effective feedback control calls for knowledge of the relationship between treatment parameters and the cavitation field dynamics. The extent to which high-fidelity bubble field modeling will play a role in this process is undetermined; it may be possible to develop systems based on purely empirical models. Regardless, the development of effective feed-back control schemes married to rules for interpreting sensor data is an important task looking forward.

A third critical barrier so the safe and effective use of cavitation for therapy involves biological effects. Not enough is known about the ways that cavitating bubbles interact with blood and tissues to yield both desirable and deleterious biological effects. Fluid transport effects, micro-jets, shock waves, even ionizing radiation are all associated with various types of cavitation activity. There is substantial evidence that cavitation can play a role in sonoporation, cell- and thrombo-lysis, ablation, coagulation, hemostasis, and even photodynamic therapy. Whether bubbles are desirably or detrimental depends on the nature of the cavitation, the extent of the cavitation, and the biological system under treatment. To move forward, we require an improved understanding of the biological consequences of cavitation for specific systems of interest.

There are a number of other areas in which a lack of knowledge presents barriers to continued progress. The list is long, and includes issues related to acoustic propagation (e.g. the role of bubble shielding), nucleation (e.g. how does one get the process started), material properties (e.g. temperature-dependent tissue rheology, the role of vapor pressure), sensing technology (e.g. imaging the bubble field, imaging the temperature field), and methodology (e.g. the use of streaming or radiation pressure to promote desired effects). Which processes and physical effects serve as technology barriers or enablers is largely application specific. It is our hope that the concepts articulated in this Chapter provide a foundation for broader understanding of therapeutically-relevant cavitation phenomena and for the continued development of the state of the art.

Acknowledgements

The authors would like to acknowledge the efforts of former and current students and research associates whose work is featured in this Chapter: Patrick Edson, Jinlan Huang, Xinmai Yang, Caleb Farny, Tianming Wu, Charles Thomas, and Constantin C. Coussios. We also point to valuable discussions with colleagues: Robin O. Cleveland, Charles C. Church, and Lawrence A. Crum, among others. Finally, the authors acknowledge the

generous financial support of our primary research sponsors: the Defense Advanced Projects Agency, the United States Army (award number DAMD17-02-2-0014, for which The U.S. Army Medical Research Acquisition Activity, 820 Chandler Street, Fort Detrick, MD is the awarding and administering acquisition office*), and the Center for Subsurface Sensing and Imaging Systems (funded under the Engineering Research Centers Program of the National Science Foundation; award number EEC-9986821).

**The content of the information in this Chapter does not necessarily reflect the position or the policy of the United States government.*

References

1. Vaezy S, Martin R, Schmiedl U, Caps M, Taylor S, Beach K, Carter S, Kaczkowski P, Keilman G, Helton S, Chandler W, Mourad P, Rice M, Roy R, Crum L: Liver hemostasis using high-intensity focused ultrasound. Ultrasound in Medicine and Biology 1997;23:1413-1420.
2. Vaezy S, Martin R, Crum L: High intensity focused ultrasound: A method of hemostasis. Echocardiography-a Journal of Cardiovascular Ultrasound and Allied Techniques 2001;18:309-315.
3. ter Haar GR: High intensity focused ultrasound for the treatment of tumors. Echocardiography-a Journal of Cardiovascular Ultrasound and Allied Techniques 2001;18:317-322.
4. Brayman AA, Azadniv M, Cox C, and Miller MW. Hemolysis of albunex-supplemented, 40% hematocrit human erythrocytes in vitro by 1 MHz pulsed ultrasound: acoustic pressure and pulse length dependence. Ultrasound in Medicine and Biology 1996; 22: 927-938.
5. Poliachik SL, Chandler WL, Mourad PD, Bailey MR, Bloch S, Cleveland RO, Kaczkowski P, Keilman G, Porter T, and Crum LA. Effect of high-intensity focused ultrasound on whole blood with and without microbubble contrast agent. Ultrasound in Medicine and Biology 1999; 25: 991-998.
6. Miller DL and Gies RA. Enhancement of ultrasonically-induced hemolysis by perfluorocarbon-based compared to air-based echo-contrast agents. Ultrasound in Medicine and Biology 1998; 24: 285-292.
7. Miller MW, Everbach EC, Cox C, Knapp RR, Brayman AA, and Sherman TA. A comparison of the hemolytic potential of Optison and Albunex in whole human blood in vitro: acoustic pressure, ultrasound frequency, donor and passive cavitation detection considerations. Ultrasound in Medicine and Biology 2001; 27: 709-721.
8. Ng KY, Liu Y. Therapeutic ultrasound: Its application in drug delivery. Medicinal Research Reviews 2002;22(2):204-223.
9. Lauer C, Burge R, Tang DB, Bass BG, Gomez ER, Alving BM. Effect of Ultrasound On Tissue-Type Plasminogen Activator-Induced Thrombolysis. Circulation 1992;86:1257-64.
10. Francis CW, Onundarson PT, Carstensen EL, Blinc A, Meltzer RS, Schwarz K, Marder VJ. Enhancement of Fibrinolysis In Vitro by Ultrasound. Journal of Clinical Investigations 1992;90:2063-2068.

11. Culp WC, Porter TR, McCowan TC, Roberson PK, James CA, Matchett WJ, Moursi M: Microbubble-augmented ultrasound declotting of thrombosed arteriovenous dialysis grafts in dogs. Journal of Vascular and Interventional Radiology 2003;14:343-347.
12. Devcic-Kuhar B, Pfaffenberger S, Groschl M, Kollmann C, Benes E, Gottsauner-Wolf M: In vitro thrombolysis enhanced by standing and travelling ultrasound wave fields. Ultrasound in Medicine and Biology 2002;28:1181-1187.
13. Adler Y, Dagan A, Golovchiner G, Iakobishvili Z, Matz I, Lev E, Siegel RJ, Birnbaum Y: Augmentation of low-frequency ultrasound-induced clot disruption by hydroxyethyl starch is dependent on the duration and intensity of ultrasound exposure; An in vitro study. Ultrasound in Medicine and Biology 2003;29:483-486.
14. Alexandrov AV, Demchuk AM, Hill MD, Felberg RA, Chernyshev O, Garami Z, Razumovsky AY, Wojner AW, Grotta JC: CLOTBUST: Phase I data on ultrasound enhanced thrombolysis for stroke. Stroke 2002;33:72.
15. Williams A, Kubowicz G, Cramer E, Schlief R: The effects of the microbubble suspension SHU 454 (Echovist) on ultrasound-induced cell-lysis in a rotating tube exposure system. Echocardiography-a Journal of Cardiovascular Ultrasound and Allied Techniques 1991;8:423-433.
16. Carstensen EL, Kelly P, Church CC, Brayman AA, Child SZ, Raeman CH, Schery L: Lysis of Erythrocytes by Exposure to CW Ultrasound. Ultrasound in Medicine and Biology 1993;19:147-165.
17. Everbach EC, Makin IRS, Azadniv M, Meltzer RS: Correlation of ultrasound-induced hemolysis with cavitation detector output in vitro. Ultrasound in Medicine and Biology 1997;23:619-624.
18. IEEE Transactions on Ultrasonics Ferroelectrics and Frequency Control 1996;43: No(6).
19. Fry WJ, Wulff VJ, Tucker D, Fry FJ. Physical factors involved in ultrasonically-induced changes in living systems: I. Identification of non-temperature effects. Journal of the Acoustical Society of America 1950; 22:867-876.
20. ter Haar GR, Daniels S, Eastaugh KC, Hill CR. Ultrasonically induced cavitation in vivo. British Journal of Cancer 1982; 45 (Suppl. V):151-155.
21. Fry FJ, Sanghvi T, Foster RS, et al. Ultrasound and microbubbles: their generation, detection and potential utilization in tissue and organ therapy -- experimental. Ultrasound in Medicine and Biology 1996;21:1227-1237.
22. Smith NB, Hynynen K. The feasibility of using focused ultrasound for transmyocardial revascularization. Ultrasound in Medicine and Biology 1998;24:1045-1054.
23. Chapelon J-Y, Prat F, Delon C, Margonari J, Gelet A, Blanc E. Effects of cavitation in the high intensity therapeutic ultrasound. Proceedings of the IEEE Ultrasonics Symposium 1991; 1357-1360.
24. Chapelon JY, Dupenloup F, Cohen H, Lenz P: Reduction of cavitation using pseudorandom signals. IEEE Transactions on Ultrasonics Ferroelectrics and Frequency Control 1996;43:623-625.
25. Chapelon J-Y, Cathignol D, Cain C, Ebbini E, Kluiwstra J-U, Sapozhnikov OA, Fleury G, Berriet R, Chupin L, Guey J-L. New piezoelectric transducers for therapeutic ultrasound. Ultrasound in Medicine and Biology 2000;26:153-159.

26. Holt RG, Roy RA: Measurements of bubble-enhanced heating from focused, MHz-frequency ultrasound in a tissue-mimicking material. Ultrasound in Medicine and Biology 2001;27:1399-1412.
27. Holt RG, Roy RA, Edson PA, Yang X: Bubbles and HIFU: The Good, the Bad, and the Ugly; in M.A. A, Crum L, Vaezy S (eds): 2nd International Symposium on Therapeutic Ultrasound. Seattle, WA, American Institute of Physics, 2002, pp 120-131.
28. Lele PP. Effects of ultrasound on solid mammalian tissues and tumors in vivo. In Repacholi MH, Grandolfo M, Rindi A, eds. Ultrasound: Medical applications, biological effects and hazard potential. New York: Plenum 1987:275-306.
29. Hynynen K. The threshold for thermally significant cavitation in dog's thigh muscle in vivo. Ultrasound in Medicine and Biology 1991;17:157-169.
30. Sanghvi NT, Hynynen K, Lizzi FL: New developments in therapeutic ultrasound. Ieee Engineering In Medicine And Biology Magazine 1996;15:83-92.
31. Clarke RL, ter Haar GR: Temperature rise recorded during lesion formation by high-intensity focused ultrasound. Ultrasound in Medicine & Biology 1997;23:299.
32. Strickberger SA, Tokano T, Kluiwstra J, Morady F, Cain C: Extracardiac ablation of the canine atrioventricular junction by use of high-intensity focused ultrasound. Circulation 1999;100:203-208.
33. Xu Z, Ludomirsky A, Eun L, Hall T, Tran BC, Fowlkes JB, Cain C: Controlled ultrasound tissue erosion. IEEE Transactions of Ultrasonics, Ferroelectrics, and Frequency Control 2004;51:726-736.
34. Sokka SD, King R, Hynynen K: MRI-guided gas bubble enhanced ultrasound heating in in vivo rabbit thigh. Physics in Medicine and Biology 2003;48:223-241.
35. Melodelima D, Chapelon JY, Theillere Y, Cathignol D: Combination of thermal and cavitation effects to generate deep lesions with an endocavitary applicator using a plane transducer: Ex vivo studies. Ultrasound in Medicine and Biology 2004;30:103-111.
36. Parker KJ. J. Acoust. Soc. Am. 1983; 74:1356-1361.
37. W. L. Nyborg, "Solutions of the Bio-Heat Transfer Equation," Phys. Med. Biol. 33 (7), 785-792 (1988).
38. Clarke RL, ter Haar GR. Ultrasound Med. Biol. 1997; 23:299-306.
39. J. Huang, R. G. Holt, R. O. Cleveland et al., "Experimental validation of a tractable numerical model for focused ultrasound heating in flow-through tissue phantoms," J. Acoust. Soc. Am. 116 (4), 2451-2458 (2004).
40. M. F. Hamilton, and C. L. Morfey. Model equations. In: M. F. Hamilton, and D. T. Blackstock, editors, Nonlinear Acoustics, Chapter 3, Academic Press, 1998.
41. Chavrier F, Chapelon JY, Gelet A, Cathignol D. Modeling of high-intensity focused ultrasound-induced lesions in the presence of cavitation bubbles. J. Acoust. Soc. Am. 108(1),432-440, (2000).
42. P. L. Edson. The Role of Acoustic Cavitation in Enhanced Ultrasound-Induced Heating in a Tissue-Mimicking Phantom, PH. D. dissertation, Boston University, 2001.
43. X. Yang. Investigation of Bubble Dynamics and Heating During Focused Ultrasound Insonation in Tissue-mimicking Materials. PhD Thesis, Boston University, 2003.

44. A. D. Pierce. Acoustics, An introduction to its physical principles and applications, Chap 10, McGraw-Hill Book Company, 1981.
45. W.L. Nyborg. Sonically produced heat in a fluid with bulk viscosity and shear viscosity. J. Acoust. Soc. Am., 80, 1133 - 1139, 1986.
46. H. H. Pennes. Analysis of tissue and arterial blood temperatures in the resting human forearm. J. Appl. Physiol., **2**, 93-122, 1948.
47. O. V. Rudenko, and S. I. Soluyan. Theoretical Foundations of Nonlinear Acoustics, Chap 8, Plenum, New York, 1977.
48. C. Eckart. Vortices and streams caused by sound waves. Phys. Rev., **73**, 68-76, 1948.
49. T. Kamakura, M. Matsuda, Y. Kumamoto, and M. A. Breazeale. Acoustic streaming induced in focused Gaussian beams. J. Acoust. Soc. Am., **97**, 2740-2746, 1995.
50. K. Matsuda, T. Kamakura, and Y. Kumamoto. Buildup of acoustic streaming in focused beams. Ultrasonics, **34**, 763-765, 1996.
51. J. Huang, Heating in Vascular and Flow-Through Tissue Phantoms Induced by Focused Ultrasound, Ph.D. Dissertation, Boston University, 2002.
52. W.L. Nyborg et al., " Bubble detection and cavitation monitoring", ANSI Technical Report S1.24 TR-2002. New York: Acoustical Society of America, (2002).
53. R. G. Holt and D. F. Gaitan, "Observation of stability boundaries in the parameter space of single bubble sonoluminescence," Phys. Rev. Lett. 77 (18), 3791-3794 (1996).
54. S. Hilgenfeldt, D. Lohse, and M. P. Brenner, "Phase diagrams for sonoluminescing bubbles," Phys. Fluids 8 (11), 2808-2826 (1996).
55. Deng CX and Lizzi FL. A review of physical phenomena associated with ultrasoniccontrast agents and illustrative clinical applications. Ultrasound in Medicine and Biology, 2002, 28, 277-286.
56. B.K. Canfield, S. Kujala, K. Jefimovs et al., "Linear and nonlinear optical responses influenced by boken symmetry in an array of gold nanoparticles," Optics Express 12 (22), 5418-5423 (2004).
57. J.-Y. Natoli, L. F. Gallais, B. Bertussi et al., "Localized pulsed laser interaction with submicronic gold particles embedded in silica: a method for investigating laser damage initiation," Optics Express 11 (7), 824-829 (2003).
58. V. Zharov and D. Lapotko, "Photothermal sensing of nanoscale targets," Rev. Sci. Instrum. 74 (1), 785-788 (2003).
59. G. Hüttmann, B. Radt, J. Serbin et al., "High precision cell surgery with nanoparticles?" Medical Laser Application 17, 9-14 (2002).
60. C.P. Lin and M.W. Kelly, "Cavitation and acoustic emission around laser-heated microparticles," Appl. Phys. Lett. 72 (22), 2800-2802 (1998).
61. C.P. Lin, M.W. Kelly, S.A.B. Sibayan et al., "Selective cell killing by microparticle absorption of pulsed laser radiation," IEEE Journal of Selected Topics in Quantum Electronics 5 (4), 963-968 (1999).
62. J. Neumann and R. Brinkmann, "Microbubble dynamics around laser heated particles," Proceedings of the SPIE Therapeutic Laser Applications and Laser-Tissue Interactions 5142 (2003).

63. C. H. Farny, T. Wu, R. G. Holt, T. W. Murray, R. A. Roy, “Nucleating cavitation from laser-illuminated nano-particles,” Acoustics Research Letters Online (accepted 2005, to appear).
64. N. A. Watkin, G. R. ter Haar, and I. H. Rivens, "The intensity dependence of the site of maximal energy deposition in focused ultraound surgery," Ultrasound in Med. & Biol., 22 (4), 483-491 (1996).
65. M. R. Bailey, L. N. Couret, O. A. Sapozhnikov et al., "Use of overpressure to assess the role of bubbles in focused ultrasound lesion shape in vitro," Ultrasound in Medicine and Biology 27 (5), 695-708 (2001).
66. S.D. Sokka, R. King, and K. Hynynen, "MRI-guided gas bubble enhanced ultrasound heating in in vivo rabbit thigh," Phys. Med. Biol. 48, 223-241 (2003).
67. D. Melodelima, J. Y. Chapelon, Y. Theillere et al., "Combination of thermal and cavitation effects to generate deep lesions with an endocavitary applicator using a plane transducer: Ex vivo studies," Ultrasound in Medicine and Biology 30 (1), 103-111 (2004).
68. Cyril Lafon, Oleg A. Sapozhnikov, Peter J. Kaczkowski et al., "An innovative synthetic tissue-mimicking material for high intensity focused ultrasound.," J. Acoust. Soc. Am. 110 (5, part 2), 2613 (2001).
69. U Parlitz, R Mettin, S Luther et al., "Spatio-temporal dynamics of acoustic cavitation bubble clouds," Philos. Trans. R. Soc. Lond. Ser. A-Math. Phys. Eng. Sci. 357, 313-334 (1999).
70. Leighton TG. The Acoustic Bubble, Academic Press, 1994.
71. J. B. Keller and M. J. Miksis, “Bubble oscillations of large amplitude,” J. Acoust. Soc. Am. **68**, 628-633 (1980).
72. A. Prosperetti and A. Lezzi, “Bubble dynamics in a compressible liquid. Part 1. First order theory,” J. Fluid Mech. **168**, 457-478 (1986).
73. Prosperetti, L. A. Crum, and K. W. Commander, “Nonlinear bubble dynamics,” J. Acoust. Soc. Am. **83**, 502-514 (1988).
74. V. Kamath and A. Prosperetti, “Numerical integration methods in gas-bubble dynamics,” J. Acoust. Soc. Am. **85**, 1538-1548 (1989).
75. I. Akhatov, N. Gumerov, C. D. Ohl et al., "The role of surface tension in stable single-bubble sonoluminescence," Phys. Rev. Lett. 78 (2), 227-230 (1997).
76. S. Hilgenfeldt, D. Lohse, and M. Zomack, “Sound scattering and localized heat deposition of pulse-driven microbubbles,” The Journal of the Acoustical Society of America **107**, 3530-3539 (2000).
77. S. Hilgenfeldt, D. Lohse, and M. Zomack, “Response of bubbles to diagnostic Ultrasound: a unifying theoretical approach,” European Physics Journal B **4**, 247-255 (1998).
78. F. Chavrier, J. Y. Chapelon, A. Gelet, and D. Cathignol, “Modeling of high-intensity focued ultrasound-induced lesions in the presence of cavitation bubbles,” The Journal of the Acoustical Society of America **108**, 432-440 (2000).
79. C. Devin, “Survey of thermal, radiation, and viscous damping of pulsating air bubbles in water,” The Journal of the Acoustical Society of America 31, 1654-1667 (1959).
80. A. Prosperetti, “Thermal effects and damping mechanisms in the forced radial oscillations of gas bubbles in liquids,” The Journal of the Acoustical Society of America **61**, 17-27 (1977).

81. M.S. Plesset, "On the stability of fluid flows with spherical symmetry," J. Appl. Phys. 25 (1), 96-98 (1954).
82. Eller A and Crum LA. Instability of the motion of a pulsating bubble in a sound field. The Journal of the Acoustical Society of America, 1970, 47, 762-767.
83. Prosperetti A. On the stability of spherically symmetric flows. Atti Accad. Naz. Lincei, Rend. Cl. Sci. Fis. Mat. Nat. 62, 1977c, 196-203.
84. Hilgenfeldt S, Lohse D, and Brenner MP. Phase diagrams for sonoluminescing bubbles. Physics of Fluids, 1996, 8, 2808-2826.
85. Hao Y and Prosperetti A. The effect of viscosity on the spherical stability of oscillating gas bubbles. Physics of Fluids, 1999, Vol. 11, (6) 1309-1317.
86. Holt RG and Gaitan DF. Observation of stability boundaries in the parameter space of single bubble sonoluminescence. Physical Review Letters, 1996, 77 (18) 3791-3794.
87. Gaitan DF and Holt RG. Experimental observations of bubble response and light intensity near the threshold for single bubble sonoluminescence in an air-water system. Physical Review E, 1999, 59, 5495-5502.
88. Prosperetti A and Hao Y. Modeling of spherical gas bubble oscillations and sonoluminescence. Philosophical Transactions of The Royal Society of London Series A, 1999, 357, 203-223.
89. Nayfeh AH and Mook DT. Nonlinear Oscillations. Wiley, John & Sons, 1995.
90. Lauterborn W. Numerical investigation of nonlinear oscillation of gas bubbles in liquids. The Journal of the Acoustical Society of America, 1976, 59, 283-293.
91. Parlitz U, Englisch V, Scheffczyk C, and Lauterborn W. Bifurcation structure of bubble oscillations. The Journal of the Acoustical Society of America, 1990, 88, 1061-1077.
92. Faraday M. On the forms and states assumed by fluids in contact with vibrating elastic surfaces. Philosophical Transactions A of The Royal Society, 1831, 121, 319-340.
93. Benjamin TB and Ursell F. The stability of the plane free surface of a liquid in vertical periodic motion. Proceedings of The Royal Society, 1954, A225, 505-515.
94. Lamb H. Hydrodynamics. Dover Publications, Inc., 1945, New York.
95. Eller A and Flynn HG. Rectified diffusion during nonlinear pulsations of cavitation bubbles. The Journal of the Acoustical Society of America, 37, 1965, 493-503.
96. Crum LA. Measurements of the growth of air bubbles by rectified diffusion. The Journal of the Acoustical Society of America, 1980, 68, 203-211.
97. Kamath V and Prosperetti A. Mass transfer during bubble oscillations. In Frontiers of Nonlinear Acoustics: Proceedings of the Twelfth International Symposium, On Nonlinear Acoustics (ed. M. F. Hamolton & D. T. Blackstock), 1990, 503-508. Elsevier.
98. Eller A. Growth of bubbles by rectified diffusion. The Journal of the Acoustical Society of America, 1969, 46, 1246-1250.
99. Fyrillas MM and Szeri AJ. Dissolution or growth of soluble spherical oscillating bubbles. Journal of Fluid Mechanics, 277, 1994, 381-407.
100. Wood AB. A Textbook of Sound. MacMillan, New York, 1st edition, 1930.
101. Commander, K. W and Prosperetti, A, "Linear pressure waves in bubbly liquids: Comparison between theory and experiments", J. Acoust. Soc. Am. 85. 723-746, 1989.